UNIVERSITÁ DEGLI STUDI DI PADOVA

DIPARTIMENTO DI FISICA E ASTRONOMIA GALILEO GALILEI

CORSO DI LAUREA MAGISTRALE IN FISICA

Spatial and Time Clustering of the High-Energy Photons collected by the Fermi LAT

Relatore:
Prof. Denis Bastieri

Laureanda:
Denise Costantin

Correlatore:
Dott. Sara Buson

Anno Accademico: 2015-2016

Contents

Introduction **6**

1 *Fermi* Gamma Ray-Space Telescope **9**
1.1 Gamma-ray Burst Monitor (GBM) 10
1.2 Large Area Telescope (LAT) 11
1.2.1 Silicon Traker 12
1.2.2 Electromagnetic Calorimeter 12
1.2.3 Anticoincidence Detector 13
1.2.4 Trigger and Data Acquisition 14
1.3 LAT Passes and Event Level Analysis 14
1.3.1 LAT Event Reconstruction 15
1.3.2 LAT Instrument Response Function 17
1.3.3 Background Rejection and Event Classification 21

2 *Fermi* LAT observed Very High Energy (VHE) γ-ray Sources **25**
2.1 Gamma-ray Sources 25
2.1.1 Diffuse Emission 25
2.1.2 Extragalactic γ-ray background 27
2.1.3 Galactic sources 27
2.1.4 Extragalactic sources 28
2.2 Mechanisms of production of γ-rays 28
2.2.1 Synchrotron Radiation 28
2.2.2 Inverse Compton Scattering 29
2.2.3 Bremsstrahlung 30
2.2.4 Pion decay 30
2.3 Active Galactic Nuclei (AGNs) 30
2.3.1 Structure 32
2.3.2 The Black Hole paradigm 32
2.3.3 AGNs Classification 33
2.3.4 Blazars, a subclass of AGNs 35
2.4 Catalogs of γ-ray Sources 36

3 Data Analysis **40**
3.1 Data Selection 40
3.2 C and Python Scripts 41
3.2.1 Clustering Algorithm 41
3.2.2 Clusters' Merging 46
3.2.3 Time Sliding Window 49
3.3 Clustering Issue 49
3.4 Maximum Likelihood Analysis of LAT Data 50

3.4.1 Likelihood analysis for photon-counting experiments 50
3.4.2 *Fermi Tools* Likelihood Analysis 52

4 Results **56**
4.1 TeVCat Catalogue Sources 56
4.1.1 4C +21.35 56
4.1.2 PKS 1441+25 57
4.1.3 PKS 1510-089 57
4.1.4 S4 0954+65 58
4.1.5 3C 279 58
4.1.6 3C 454.3 59
4.2 Known identified Flares 60
4.2.1 B0218+357 61
4.2.2 GRB 130427A 61
4.3 New Sources 62

5 Conclusion **64**

Bibliography **66**

List of Tables

1.1 Detail of event classes classification. 23

2.1 AGN classification based on both the radio-loudness and the optical properties of the sources. 34
2.2 3FGL catalog sources. The population of sources in 3FGL is dominantly unassociated, followed by BL Lac blazars (Acero et al., 2015 [4]). 38
2.3 2FHL catalog sources (Ackermann M. et al., 2015 2.3). 39

3.1 Selection criteria for the data to which the clustering analysis was applied. 41
3.2 Cut on theta values that we choose for different PSF quartiles. . . . 45
3.3 Selection data for the Unbinned Likelihood Analysis. 53

4.1 Clusters associate with B0218+357 source, looking at a time range of 2 days, between (426954901 - 427127701) in MET. 61

List of Figures

1 Angular resolution for Fermi-LAT and CTA. H.E.S.S. and HAWC and Energy resolution for *Fermi* LAT CTA and HAWC. 7

1.1 Energy coverage of GLAST LAT and GBM. 10
1.2 Schematic display of the LAT. 12
1.3 LAT calorimeter module. 13
1.4 Example of a ghost event in the LAT ($y-z$ orthogonal projection). 16
1.5 The effective area for Fermi LAT as described by the $P8R2\_V6$ IRF, `SOURCE`. 19
1.6 The acceptance of Fermi-LAT described by $P8R2\_V6$ IRF, `SOURCE` class. 19
1.7 Containment angles at 68% and 95% of the acceptance weighted PSF for PSF event types. 20
1.8 Comparison between `P7REP_SOURCE_V15` and `P8R2_SOURCE_V6` performance measures. 21

2.1 The Fermi LAT 60-month image, constructed from front-converting gamma rays with energies greater than $1\,GeV$. 26
2.2 Synchrotron spectrum emitted in a typical astrophysical source. . . . 29
2.3 Graphic representation of an AGN with only one jet, as described by the modern Unifying Theory. 31
2.4 The blazar sequence concept of Fossati et al., 1998 36
2.5 Sky map, in Galactic coordinates and Hammer-Aitoff projection, showing the sources in the 2FHL catalog classified by their most likely association. 39

3.1 This figure defines the (θ, ϕ) coordinate system used. 42
3.2 Containment angles at 95% of the acceptance weighted (acc. weighted) PSF for PSF event types of the characteristic $P8R2\_V6$ IRFs, `SOURCE` class. 43
3.3 The effective area for Fermi LAT as described by the $P8R2\_V6$ IRF, `SOURCE` class; as a function of incidence angle theta for 10 GeV photons. 44
3.4 Containment angle at 95% of a fixed PSF quartile in function of θ inclination angle. 45
3.5 Clusters Radius and Numerosity in function of different photon type of seed. 48
3.6 Wrong Clusters Distribution in galactic coordinate. 50
3.7 Histogram of photons galactic longitude collected by *Fermi* LAT. . . 50

4.1 Temporal variability of FSRQ of TeVCat Catalogue. 60

4.2 Clusters obtained by a data set with a range in time between [386968129 – 389560129] in MET. We highlight with a circle the GRB 130427A cluster localization (RA= 173.15°; DEC= 27.71°) with 18 photons within the cluster and a small radius 0.13°, thus a small dispersion. . 62
4.3 Clusters obtained by a data set with a range in time between [272920129-275512129] in MET. We highlight with a circle the cluster localization (RA= 264.93°; DEC= 27.34°) with 7 photons within the cluster and a small radius 0.14°, thus a small dispersion. 63
4.4 Clusters obtained by a data set with a range in time between [441400129-443992129] in MET. We highlight with a circle the cluster localization (RA= 159.50°; DEC= 45.09°) with 4 photons within the cluster and a small radius 0.14°, thus a small dispersion. 63

Introduction

The *Fermi* Gamma-ray Space Telescope (Fermi), launched on June 11th 2008, began its first year sky survey on August 11th 2008. The primary instrument onboard *Fermi* is the Large Area Telescope (LAT), a wide field-of-view pair-conversion telescope covering the energy range from 20 MeV to more than 300 GeV. (Atwood et al., 2009 [16]).
This thesis is a work based on the data collected by the LAT from October 29th 2008 to January 11th 2016, processed in the context of the Pass 8 version of the of the LAT event-level analysis.
The release of the new *Fermi* LAT data processed Pass 8 provides a full reprocessing of the entire mission dataset, including improved event reconstruction, a wider energy range, better energy measurements, and significantly increased effective area. In addition, the events have been evaluated for their measurement quality in both position and energy. This allows to select a subset of the events if appropriate to improve analysis results. All these enhancements lead to a significant increase of the LAT sensitivity and its effective energy range, from $20\,MeV$ to $> 300\,GeV$.
This work's aims are two. On the one hand, we are interested to identify new potential γ-ray sources, with special focus on the high-energy (HE, $> 10\,GeV$), which are the best candidate to be very-high-energy (VHE, $> 100\,GeV$) emitters. On the other hand we study γ-ray properties of known HE sources, such as the variability. We analyse the whole *Fermi* LAT data set (about 7 years) as well as study shorter-time interval datasets, using a spatial and time clustering analysis. A study of shorter time interval dataset allows both to study the temporal variations of the luminous flux of known high-energy sources and to point out sources that underwent a flare of short duration. The latter ones would likely miss a detection when considering broader time intervals, since their signal-to-noise will be too low.
In this work we analyse the energy range between 10 GeV and 1 TeV, at these energies extragalactic Universe is dominated by Active Galactic Nuclei (AGNs), in particular by a subclass of AGNs, strongly variable sources, dubbed Blazars, whose jet is aligned with the line of sight.
It is important to analyse this energy range, in fact it is where space-based detectors such as the *Fermi* LAT and ground-based instruments such as the next-generation Cherenkov Telescope Array (CTA) overlap. We are able to study the *Fermi* LAT gamma sky until few TeV, and thus we have an increased overlap in energy coverage between CTA and *Fermi* LAT, thanks to Pass 8 data release.
In fact since CTA has a huge discovery potential over the *Fermi* LAT in the overlapping energy range for short-transient phenomena due to the huge collection area (typically 10^5 larger than the LAT effective area); the *Fermi* LAT has the advantage of a 2.4 sr field of view which makes catching transients much more likely. In addition, the *Fermi* LAT can view gamma rays out to much larger redshifts due to the $\gamma\gamma$ pair production opacity of the Universe at higher gamma-ray energies. (Funk and

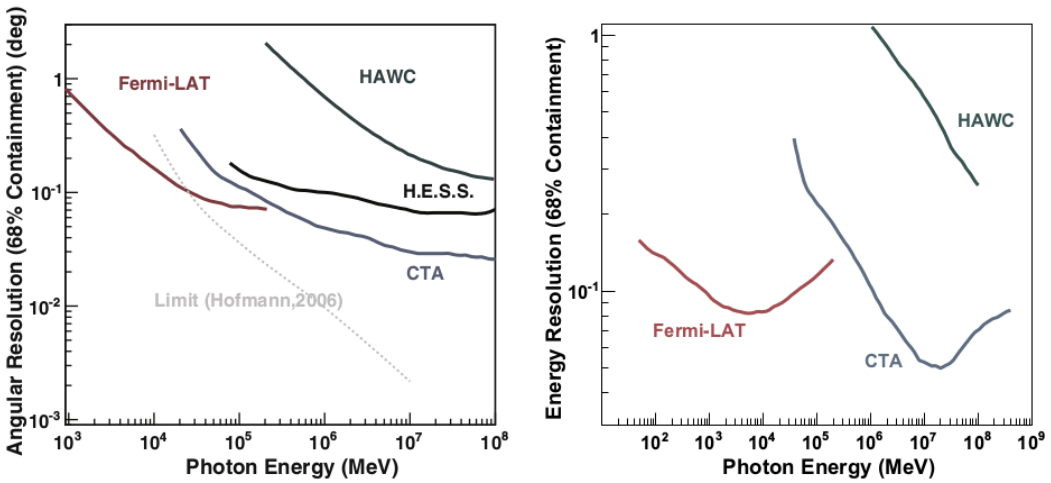

Figure 1: Angular resolution for Fermi-LAT and CTA. H.E.S.S. and HAWC are shown as examples for a current-generation IACT and for a next-generation water Cherenkov detector. Also shown is the limiting angular resolution that could be achieved if all Cherenkov photons emitted by the particle shower could be detected. The CTA curve has not been optimized for angular resolution and enhanced analysis techniques are expected to improve this curve. Right: Energy resolution for *Fermi* LAT and CTA. Shown is the 68% containment radius around the mean of the reconstructed energy. It is evident that the energy resolution of Fermi-LAT in the overlapping energy range is significantly better than the CTA resolution.(Funk and Hinton, 2013 [28])

Hinton, 2013 [28])
However, contrary to the *Fermi* LAT, CTA in the overlapping energy range, is dominated by the systematic uncertainties. Therefore longer observations do not help the CTA sensitivity in this range.
Using a spatial and time clustering algorithm we produce a list of sources that are ideal candidates for VHE emitters that will constitute the best targets for the narrow field-of-view Cherenkov detectors, that will be particularly useful and important in light of the forthcoming Cherenkov Telescope Array (CTA). Thus with this work what we are aiming is to increase the so far restricted population of VHE emitters that will provide a cross-calibration for ground-based instruments.
Moreover, with the detection and the study of new VHE objects, we will be able to improve our understanding of VHE γ-ray Active Galactic Nuclei (AGN). The study of Very Hight Energy (VHE) sources is very interesting, since it allows us to observe the most energetic and violent processes in the Universe and, in particular, their non-thermal aspects as well as the observation of the cosmic structure formation. Lastly, another major cosmological aspect of VHE γ-ray astronomy is an indirect dark matter (DM) search through the detection of annihilation radiation from the lightest supersymmetric SUSY particles (called neutralino).
The thesis is organized as follows.
Chapter 1 provides an overview of the *Fermi* LAT technical characteristics and on the way data are selected for the analysis proposed in this work. The chapter will focus also on the new event types (based on the quality of the reconstructed energy and direction) that come with the Pass 8 release.
Chapter 2 gives a general introduction of Very High Energy (VHE) γ-ray sources with special emphasis on the main observed properties and interpretations of AGNs.
Chapter 3 describes the spatial and time clustering algorithm that we developed

during this works and in Chapter 4 we describe the main results and, in particular, the application of the clustering algorithm to known sources and to detect new ones. Finally, Chapter 5 contains the conclusions and future perspective.

Chapter 1

Fermi Gamma Ray-Space Telescope

The *Fermi* Gamma-Ray Space Telescope, formerly called the Gamma-ray Large Area Space Telescope (GLAST), was launched into a low Earth orbit on 11 June 2008. The mission scientific objectives are (Atwood et al., 2009 [16]):

- Resolve the gamma-ray sky of unidentified sources and diffuse emission, in particular determine the nature of the unidentified sources and the origins of the diffuse emission revealed by EGRET (Energetic Gamma Ray Experiment Telescope - energy range from $30\,MeV$ to $30\,GeV$); of interstellar emission from the Milky Way and nearby galaxies; of extragalactic diffuse emission.
- Understand the mechanisms of particle acceleration operating in celestial sources, particularly in active galactic nuclei (AGN), pulsars, supernovae remnants (SNR), and the Sun. For example explain how black holes accelerate immense jets of material to nearly light speed.
- Understand the high energy behavior of Gamma Ray Bursts (GRBs) and transients.
- Use γ-ray observations (e.g. by looking for an excess of γ-rays from the center of the Milky Way) as a probe of Dark Matter.
- Use high-energy γ-rays to probe the early universe and the cosmic evolution of high energy sources.

In order to meet this objectives, the spacecraft is composed by two instruments: the Large Area Telescope (LAT) and the Gamma-ray Burst Monitor (GBM). Each of them cover two different energy range. In fact the LAT is a wide-field gamma-ray telescope and covers an energy range between $20\,MeV - 300\,GeV$, then with Pass8 until $2\,TeV$. Whereas the GBM complements the LAT in its observations of transient sources and is sensitive to X-rays and gamma rays with energies between $8\,keV - 40\,MeV$.

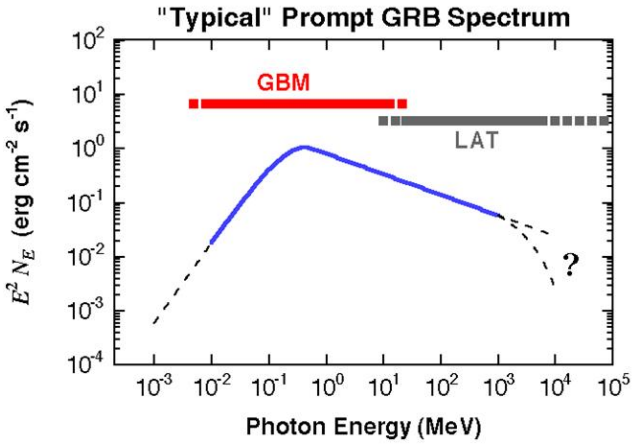

Figure 1.1: Energy coverage of GLAST LAT and GBM: the range of sensitivity of each instrument is shown on top of a sample GRB spectrum; a possible spectral break within the LAT range is shown.

The *Fermi* observatory is very flexible in the direction in which it can point. An observational constraint is to avoid pointing at or near the Earth, the so called Earth's limb is indeed a very strong source of albedo γ-rays, which the LAT may occasionally observe for instrument calibration. Another constraint is to stop observation when *Fermi* is flying over the South Atlantic Anomaly (SAA), a region over the South Atlantic with a high density of charged particles that are trapped by the configuration of the Earth's magnetic field. In a 25.6° inclination orbit and at Fermi's altitude, SAA outages cost 15% of the LAT's and GBMs potential observing time.
Therefore the Fermi spacecraft supports a variety of different types of observations. The most common mode for the spacecraft is *all-sky survey*, where the observatory scans across a hemisphere of the sky for one orbit, then rocks to the other hemisphere to scan for the second orbit. Every two orbits (3 hours) this pointing mode will provide at least 30 minutes of livetime observations on each direction of the sky. Since the start of science operations of the Fermi mission in August 2008, this observational mode was the default mode.
It has different modes of pointed observations. An autonomous repoint request can be sent to the spacecraft in order to change the observing mode to monitor the location of a GRB (or other short timescale transient) in or near the LAT's FOV and pre-scheduled pointed observations may be part of the normal science timeline. This mode keeps the earth out of the FOV; the default Earth Avoidance Angle, defined as the minimum angle between the LAT axis and the Earth's limb, is 30 degrees.
In addition it may combine or modify the survey and observation modes in order to execute alternate observing strategies that more effectively accommodate specific science drivers, such as a desire for increased sensitivity to flaring sources in the northern hemisphere, or monitoring sources near the galactic center.

1.1 Gamma-ray Burst Monitor (GBM)

The GLAST Burst Monitor detects sudden flares of gamma-rays produced by gamma ray bursts and solar flares. Its scintillators are on the sides of the spacecraft to view all of the sky which is not blocked by the Earth.
It includes 12 Sodium Iodide (NaI) scintillation detectors and 2 Bismuth Germanate (BGO) scintillation detectors. NaI detectors cover the lower part of the energy range,

from a few keV to about $1\,MeV$ and provide burst triggers and locations. While BGO detectors cover the energy range of $\sim 150\,keV$ to $\sim 30\,MeV$, providing a good overlap with the NaI at the lower end, and with the LAT at the high end.
Although both the detectors have similar characteristics to the combination of the BATSE (Burst and Transient Source Experiment) large area and spectroscopy detectors, they cover a wider energy range and have a smaller collection area.
The 12 NaI detectors are directly coupled to a photomultiplier tube (PMT), they provide spectral coverage from about $8\,keV$ to $1\,MeV$. NaI is an ideal scintillation material for this energy range combining low cost, high efficiency, and adequate spectral resolution. The thickness ($1.27\,cm$) of the detectors is optimum for the energy range where bursts typically emit the most energy and provides approximately a cosine angular response, which is important for determining locations using relative rates, similar to BATSE. Lower energy coverage relative to BATSE is obtained by using a $0.25\,mm$ beryllium window to the detectors. The detectors are arranged in 4 banks of 3 detectors so that the larger number of detectors, each viewing a smaller field-of-view, reduces systematic errors for burst locations and allow an improved triggering algorithm.
Each of the 2 BGO detectors is viewed by 2 PMTs for improved resolution and redundancy. Since BGO is a high-density material which provides good sensitivity over this difficult energy range, BGO detectors provide spectral coverage from about $150\,keV$ to $40\,MeV$. The energy resolution of the $12.7\,cm$ by $12.7\,cm$ cylindrical BGO crystal is 14% at $661\,keV$ and 4% at $10\,MeV$ and there is significant overlap with the lower energy range of the LAT. Each BGO detector is coupled to 2 PMTs on opposite sides, whose outputs are summed, each with its own high-voltage control. This design allows a homogeneous light collection over the detector volume and also provides redundancy should one of the PMT's fail or degrade. The BGO detectors are positioned on opposite sides of the LAT, providing nearly full sky coverage.

1.2 Large Area Telescope (LAT)

The Large Area Telescope (LAT) is the principal scientific instrument on the Fermi Gamma Ray Space Telescope spacecraft. The LAT is designed to measure the directions, energies, and arrival times of γ-rays incident over a wide field of view (FoV), while rejecting background from cosmic rays.
It is a kind of detector called a pair-conversion telescope; individual γ-rays hit thin metal sheets (converter) made of a high Z material, Tungsten in our case, to produce $e^+\,e^-$ pairs, which are recorded by the instrument. (Atwood et al., 2007 [15])
By reconstructing the $e^+\,e^-$ pair we can deduce the direction and energy of the incident γ-ray. The pair is tracked through the instrument by using Silicon Strip Detectors (SSD). Since the gamma-ray energy is much larger than the rest mass of the electron and positron, both members of the pair continue predominantly in the direction of the incident gamma ray. So the reconstructed direction on the incoming gamma-ray is limited by multiple scatterings of the pair components in the tracker material as well as the spatial resolution of the tracker. Located at the bottom of the LAT, a calorimeter made of CsI(Tl) (scintillator crystals made of Caesium Iodide doped with Thallium), thick enough, provides an adequate energy measurement of the pairs in the LAT energy band.
Both the tracker (TKR) and the calorimeter (CAL) consist of 16 modules, often referred to as towers, arranged in a 4×4 grid. Each tower has a footprint of $\sim 37\,cm \times 37\,cm$ and is $\sim 85\,cm$ high. (Atwood et al., 2009 [16])

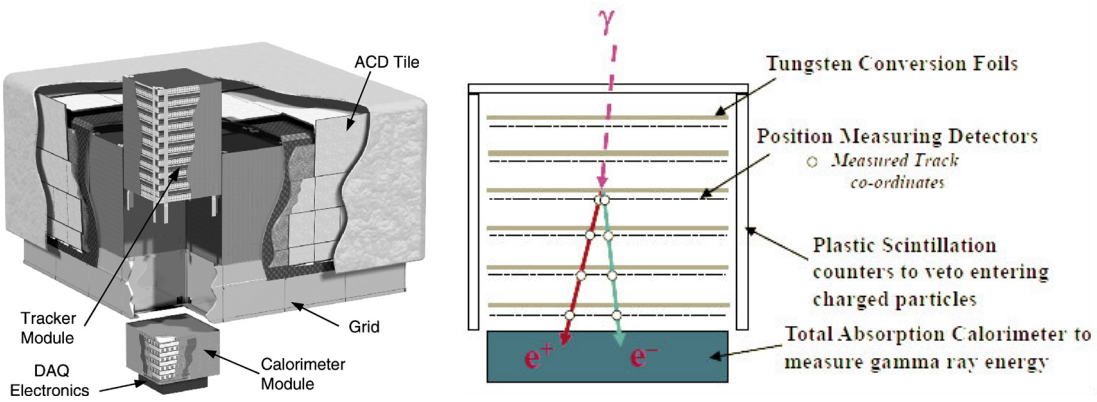

Figure 1.2: LAT structure. On the left hand we look a structure where the single modules are visible, thanks to a cut on a tower. On the right hand we look a schematic picture of each LAT modules with its function indicated.

1.2.1 Silicon Traker

The tracker (TKR) is a 18 layers of paired x–y SSD planes with interleaved tungsten foils, which promote pair conversion and measure the directions of incident particles (Atwood et al., 2007 [15]).
The TKR is effectively divided into two distinct instruments with notable differences in performance, especially with respect to the PSF and background contamination. This choice was suggested by the need to balance two basic requirements: obtaining good angular resolution and a large conversion probability. (Ackermann et al., 2012 [5]) The first 12 paired layers, from the top (farthest from the CAL), are arranged to immediately follow converter foils, which are composed of $\sim 3\%$ of a radiation length of tungsten. It is referred to as the thin or front section. The next 4 layers are similar, except that the tungsten converters are ~ 6 times thicker; these layers are referred to as the thick or back section. The tungsten foils were designed such that there are approximately the same number of γ-rays (integrated over the instrument FoV) converted in the thin and thick sections. In addition to these considerations, experience on orbit has also revealed that the aggregate of the thick layers limits the amount of back-scattered particles from the CAL returning into the TKR and ACD in high-energy events (i.e., the CAL backsplash) and reduces tails of showers in the TKR from events entering the back of the CAL. These two effects help to decrease the background contamination in front-converting events.

1.2.2 Electromagnetic Calorimeter

The Calorimeter (CAL) is a 3D imaging calorimeter, provides energy measurements as well as some imaging capability (Grove and Johnson, 2010 [30]). It is composed by CsI(Tl) scintillation crystals stacked in 8 layers, each with 12 crystal logs (with dimensions $326\,mm \times 26.7\,mm \times 19.9\,mm$) and arranged in a hodoscopic configuration. This last statement means that each layer is aligned at 90° with respect to the previous one, forming an x, y array, alike the TKR Silicon detectors. Each crystal block is read out by four photodiodes, two at each end: a large photodiode covering low energies ($< 1\,GeV$ per crystal), and a small photodiode covering high energies ($< 70\,GeV$ per crystal). Each photodiode is connected to a charge-sensitive preamplifier whose output drives: a slow shaping amplifier for spectroscopy and a fast shaping amplifier for trigger discrimination. In addition, the output of each slow shaper is connected to two separate track-and-hold stages with different gains. The outputs of the four

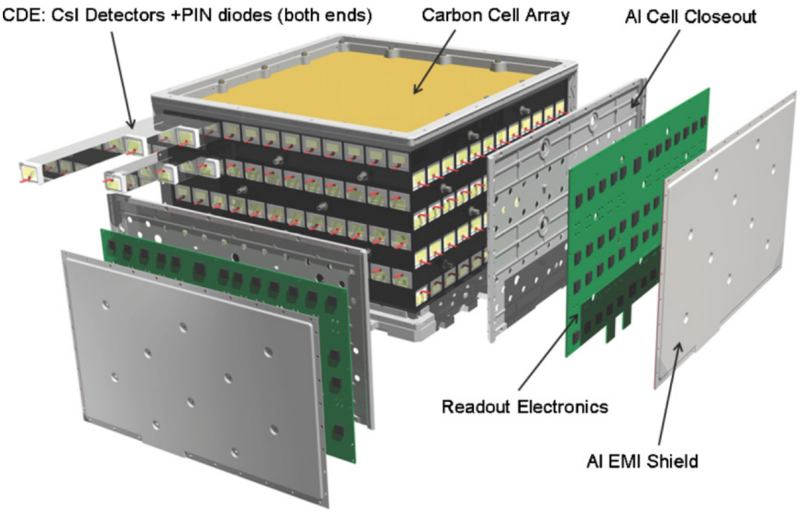

Figure 1.3: LAT calorimeter module. The 96 CsI(Tl) scintillator crystal detector elements are arranged in eight layers, with the orientation of the crystals in adjacent layers rotated by 90°.

track-and-hold stages are multiplexed to a single analog-to-digital converter. The four gain ranges (two photodiodes × two track-and-hold gains) span an enormous dynamic range, from $< 2\,MeV$ to $70\,GeV$ deposited per crystal, which is necessary to cover the full energy range of the LAT. For each log with deposited energy, two position coordinates are derived from the geometrical location of the log within the CAL array, while the longitudinal position is derived from the ratio of signals at opposite ends of the log: the crystal surfaces were treated to provide monotonically decreasing scintillation light collection with increasing distance from a photodiode. Since the CAL is only 8.6 radiation lengths thick at normal incidence, for energies greater than a few GeV shower leakage becomes the dominant factor limiting the energy resolution, in particular because event-to-event variations in the early shower development cause fluctuations in the leakage out the back of the CAL. Indeed, by $\sim 100\,GeV$ about half of the total energy in showers at normal incidence escapes out the back of the LAT on average.

1.2.3 Anticoincidence Detector

The Anticoincidence Detector (ACD), featuring an array of plastic scintillator tiles and wavelength-shifting fibers, surrounds the TKR and rejects cosmic rays backgrounds (Moiseev et al. 2007 [45]).
The ACD consists of 25 scintillating plastic tiles covering the top of the instrument and 16 tiles covering each of the four sides (89 in all). By design, the segmentation of the ACD does not match that of the LAT tower modules, to avoid lining up gaps between tiles with gaps in the TKR and CAL. The design requirements for the ACD specified the capability to reject entering charged particles with an efficiency $> 99.97\%$. The required segmentation inevitably led to less hermeticity. In fact gaps of $\sim 2.5\,mm$ are covered by bundles of scintillating fibers (called ribbons), read out at each end by a photomultiplier tube (PMT). The light yield for these ribbons, is considerably less than for the tiles, therefore, along the gaps the efficiency for detecting the passage of charged particles is lower. In addition to the gaps between ACD tile rows, the corners on the sides of the ACD have gaps that are not covered by ribbons and must be accounted for in the reconstruction and event classification.

The output of each PMT is connected both to a fast shaping amplifier for trigger purposes and two separate slow electronics chains to measure the signal amplitude.

1.2.4 Trigger and Data Acquisition

The Data Acquisition System (DAQ) collects the data from the other subsystems, implements the multi-level event trigger, provides on-board event processing to run filter algorithms to reduce the number of downlinked events, and provides an on-board science analysis platform to rapidly search for transients. At the lowest level, each of 16 Tower Electronics Modules (TEMs) provides the interface to the tracker and calorimeter pair in one of the towers. Each TEM generates instrument trigger primitives from combinations of tower subsystem (tracker and calorimeter) triggers, provides event buffering to support event readout, and communicates with the instrument-level Event Builder Module that is part of the Global-trigger/ACD-module/Signal distribution Unit (GASU). Any of the TEMs can generate a trigger request in several ways:

- If any tracker channel in the tracker module is over threshold, a trigger request is sent to the module's TEM which then checks if a trigger condition is satisfied, typically requiring triggers from 3 x, y planes in a row. If this condition is satisfied, the TEM sends a trigger request to the GEM (Global-Trigger Electronics Module).
- If a predetermined low-energy (CAL-LO) or high-energy (CAL-HI) threshold is exceeded for any crystal in the calorimeter module, a trigger request is sent to the GEM.

The trigger was designed to be efficient for γ-rays while keeping the total trigger rate, which is dominated by charged cosmic rays, low enough to limit the dead-time fraction. The triggering criteria are programmable to allow additional, prescaled event streams for continuous instrument monitoring and calibration during normal operation.

1.3 LAT Passes and Event Level Analysis

Over the course of the mission the event-level analysis software has been periodically updated to take advantage of improvements in the understanding of the LAT and its orbital environment. Therefore with *Pass* we mean a version of the Fermi LAT data, that implies a whole package of: instrument simulation, reconstruction code, event selection, Instrument Response Functions (IRFs), systematic uncertainties, isotropic template, which includes the cosmic-ray residual background.
Since launch, there have been four major releases: `Pass 6`, `Pass 7`, `Pass 7 Reprocess` and `Pass 8`. Whereas previous passes were primarily focused on reducing systematic uncertainties in the instrument response functions, `Pass 8` is a comprehensive revision of the entire analysis chain that yields substantial gains in instrument performance. It has a much more radical change in the iteration of the event analysis scheme as well in the event reconstruction; for example it uses clustering information from the CAL to minimize the effect of the *ghost* events, that are instrumental pile-up away from the gamma-ray shower which introduced errors in the measurement of the energy, and shower center and direction, during the event analysis. (Atwood et al., 2013 [17])
The LAT data that we analyse have been processed using this last released version,

that improves the event tracking and energy reconstruction, provides a better algorithm for the association between tracks and ACD tiles for the rejection of charged particles, and a new event classification analysis based on boosted decision trees that improves the separation power between photon and cosmic-ray background events.

1.3.1 LAT Event Reconstruction

The event reconstruction processes the raw data from the various subsystems, correlating them and grouping the data that could possibly originated by the same event. The reconstruction relies on the Monte Carlo simulation of the LAT's response to signals and backgrounds.

Monte Carlo Simulations

Monte Carlo simulations are important both for showing that the LAT design could achieve the necessary rejection of backgrounds expected in the observatory's orbit and for supporting the pre-launch development of software tools to backup scientific data analysis. The instrument simulation consists of 3 parts:

- particle generation and tracking use standard particle physics simulators of particle interactions in matter to model the physical interactions of γ-rays and background particle fluxes incident on the LAT
- for a given simulated event the instrument response is calculated parametrically based on the energy deposition and location in active detector volumes in the anticoincidence detector, tracker, and calorimeter
- from the digitized instrument responses, a set of trigger primitives are computed and a similar of the Trigger and On-board Flight Software Filter is applied to the simulated data stream

Thus the simulation is detailed enough to produce uncalibrated signals for each channel, in fact we maintain fidelity to the analysis of the flight data by processing simulated data with the same reconstruction and analysis algorithms as the flight data. Moreover, we simulate the data as seen by the trigger and the on-board software, and process the data with a simulation of the hardware trigger and exactly the same on-board filter algorithms as used on the LAT. So we can merge the signals from two events into a single event. We rely on this feature to add an unbiased sample of *ghost* signals to simulated events.

Ghost events

Soon after launch, it became apparent that the LAT was recording events that included an unanticipated background: remnants of electronic signals from particles that traversed the LAT a few μs before the particle that triggered the event. We refer to these remnants as ghosts.
This noise confuses the event reconstruction and led to a degraded energy or direction measurement, or even to reject incorrectly a good γ-ray event as if it were background. An example of ghost events is given in Figure 1.4. If a particle traverses the LAT a few μs before or after the instrument has entered in read out mode, it is possible that the signal it leaves in the various electronic channels are erroneously read out together with the event data.
Thanks to `Pass 8` new event reconstruction, described below, we minimize the effect of such spurious signals during the event analysis.

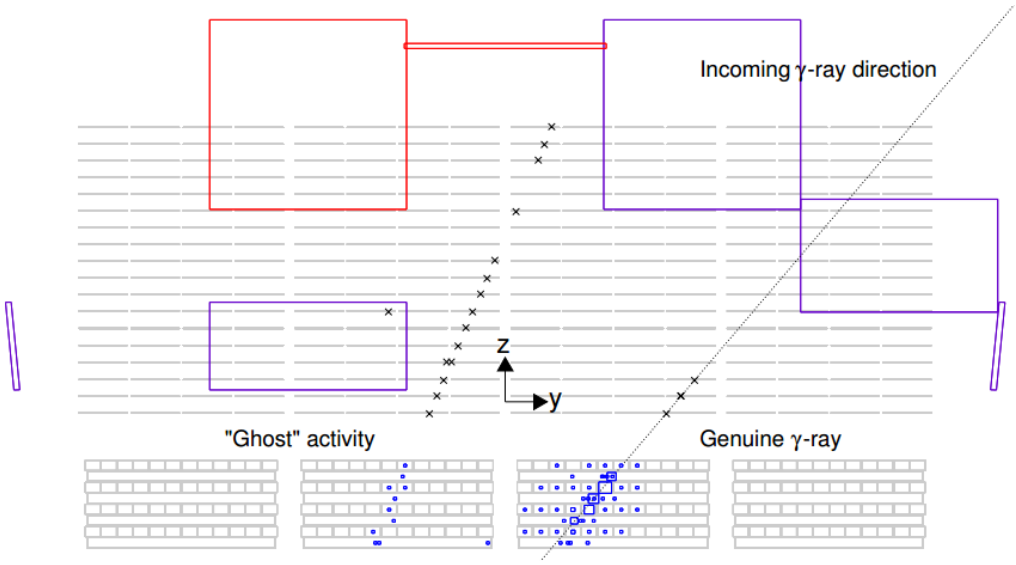

Figure 1.4: Example of a ghost event in the LAT ($y-z$ orthogonal projection). In addition to an $8.5\,GeV$ back-converting γ-ray candidate (on the right) there is additional activity in all the three LAT subsystems, with the remnants of a charged particle track crossing the ACD, TKR and CAL. The small crosses represent the clusters (i.e., groups of adjacent hit strips) in the TKR, while the variable size squares indicate the reconstructed location of the energy deposition for every hit crystal in the CAL (the side of the square being proportional to the magnitude of the energy release). The dashed line indicates the γ-ray direction. For graphical clarity, only the ACD volumes with a signal above the zero suppression level are displayed. (Abdo et al., 2009 [1]).

Track reconstruction

The `Pass 7` tracker reconstruction code uses a track-by-track combinatoric pattern recognition algorithm to find and fit up to two tracks, representing the electron-positron pair, (called *Calorimeter-Seeded Pattern Recognition* (CSPR)). This algorithm uses energy deposition information in the calorimeter and is based on the assumption that the centroid lies on the trajectory, so it uses the reconstructed CAL energy centroid and axis to choose the initial hits. (Atwood et al., 2013 [17]) A limitation of such approach is that this makes the efficiency and quality of the track-finding intrinsically dependent on the accuracy of the CAL reconstruction.
Moreover, high number of hits can confuse the track-finding algorithm. Due to both the presence of multiple hits produced by electrons and positrons interacting in the converter foils and in the silicon-strip plates, and to back-splash particles which move upwards from the calorimeter, in particular for high-energy deposition in the calorimeter, causing a large number of randomly hit strips in the lower planes of the tracker.
The `Pass-8` gives a new pattern recognition in the tracker reconstruction with a tree-based tracking, that is significantly more effective for events at high energy and large off-axis angles.
It looks at the conversion in the tracker as the start of a shower and attempts to model this process by linking hits together into one or more tree-like structures. The head of the tree is given by the assumed gamma-ray conversion point. The primary electron and positron represents the primary and secondary branches in each tree, each branch is featured by sub-branches that represent subsequent hits as the electron and positron radiate energy passing through the tracker. Then we

evaluate the axis of tree, that can be used to associate the tree to a particular cluster in the calorimeter, which allows to estimate the energy. Then the two tracks are extracted from the hits along the primary and secondary branches and fitted, taking into account multiple scattering.
If more than one track is produced from a given tree, then an attempt is made to combine the two tracks into the vertex expected in a pair conversion. The resulting vertex generally yields the best information on the photon direction.
Tests with Monte Carlo simulations and flight data show that the new tracker pattern recognition significantly reduces the fraction of mis-tracked events.

Energy reconstruction

We begin to evaluate the event energy by measure the energy depositions in the crystals. The energy deposition is treated as a single quantity with the previous event-level analysis data `Pass6` and `Pass7`, afterwards with `Pass8` there is the attempt to consider also the contamination from ghost signals, where the computation of shower centroid and axis has been preceded by a clustering-stage.
The amount of energy deposited in the TKR is evaluated by treating the tungsten-silicon detector as a sampling calorimeter; this contribution is an important correction at low energies. Three algorithms were designed to estimate the actual energy of an event in order to provide the best performance in different parts of the energy and incidence angle phase space:

- **Parametric Correction** (PC) algorithm bases on the barycenter of the shower, it covers the entire phase space of the LAT
- **Shower Profile** (SP) algorithm takes into account the longitudinal and transverse development of the shower but it does not work well for events below $\sim 1\,GeV$
- **Maximum Likelihood** (LH) algorithm bases on the correlations of the overall total energy deposited with the number of hits in the tracker and with the energy seen in the last layer. It is only tuned up to $300\,GeV$

1.3.2 LAT Instrument Response Function

A result of the performance analysis, due to the comparison between the properties of the simulated events within a given event class and the detected photons, is the production of full Instrument Response Functions (IRFs), describing the instrument performance.
The LAT team assumes that the IRFs, defined as a function R of true photon energy E' and direction $\hat{p}'$, measured photon energy E and direction $\hat{p}$, can be factorized into three parts:

$$R(E,\hat{p}|E',\hat{p}') = A_{eff}(E',\hat{p}')P(\hat{p}|E',\hat{p}')D(E|E',\hat{p}') \tag{1.1}$$

Actually a scaling factor $T(t)$ should be included in Equation 1.1, to account for temporal variations due to instrument failures or to the deterioration of instrument components. Nevertheless the lack of consumables makes the LAT performance very stable and therefore this term is negligible.

Effective Area

The Effective Area, $A_{eff}(E',\hat{p}')$, depends on the geometrical cross section of the

LAT as well as the efficiency for converting and correctly identifying incident γ-rays. The Montecarlo simulation is the main tool for evaluating A_{eff}, which is then corrected, if needed, based on comparison with flight data. Since in the simulation γ-rays are generated uniformly in $log(E)$ and solid angle, the effective area in any of the bins in which the parameter space is partitioned can be calculated from the ratio of the number of events $n_{i,j,k}$ which pass the criteria of γ-ray selection, within the specific bin centered at (E_i, θ_j, ϕ_k), to the total number of generated events N_{gen}:

$$A_{eff}(E_i, \theta_j, \phi_k) = (6m^2)\left(\frac{n_{i,j,k}}{N_{gen}}\right)\left(\frac{2\pi}{\Delta\Omega_{j,k}}\right)\left(\frac{log_{10}E_{max} - log_{10}E_{min}}{log_{10}E_{max,i} - log_{10}E_{min,i}}\right) \quad (1.2)$$

where $\Omega_{j,k}$ is the solid angle subtended by the angular bin centered on (θ_i, ϕ_k), E_{min} and E_{max} give the energy range of the simulated sample and $E_{max,i}$ and $E_{min,i}$ are the boundaries of the $i-th$ energy bin. The factor of $(6m^2)$ is the cross sectional area of the sphere where the γ-rays are simulated, which covers the LAT and the majority of the spacecraft. Like the PSF, the ϕ dependence of the A_{eff} is generally small enough to ignore for most analyses, so Eq. 1.2 can be rewritten as:

$$A_{eff}(E_i, \theta_j, \phi_k) = (6m^2)\left(\frac{n_{i,j}}{N_{gen}}\right)\left(\frac{2\pi}{\Delta\Omega_{j}}\right)\left(\frac{log_{10}E_{max} - log_{10}E_{min}}{log_{10}E_{max,i} - log_{10}E_{min,i}}\right) \times R(E_i, \theta_j, \phi_k) \quad (1.3)$$

Here, the correction factor $R(E_i, \theta_j, \phi_k)$ is a small factor (typically $< 10\%$) whose average over ϕ is 1 by construction for any E and θ.
Two important parameters that the LAT measures are obtained from the effective area. The first one is the acceptance, defined as the integral of the effective area over solid angle, given by:

$$\mathcal{A}(E) = \int A_{eff}(E, \theta, \phi) d\Omega \quad (1.4)$$

and the Field of View (FoV), at any given energy, as the ratio between the acceptance and the on-axis effective area ($\theta = 0$), by:

$$FoV(E) = \frac{\mathcal{A}(E)}{A_{eff}(E, \theta = 0)} \quad (1.5)$$

Point Spread Function

The Point Spread Function (PSF) $P(\hat{p}|E', \hat{p}')$ is the probability to reconstruct an incident direction $\hat{p}$ for a γ-ray with $E', \hat{p}'$. A standard way to summarize the angular resolution in a given region of the phase space is to compute the angular width in the space containing a certain fraction, typically 68% or 95%, this information is extracted from the PSF. (We note that the dependence from ϕ has been found to be much weaker then that from θ, so we can neglected it.)
As with the effective area and energy dispersion, the PSF is determined by Monte Carlo simulations of the detector. The most relevant factor in determining the PSF at low-energy is the multiple scattering of the primary electron-positron pair in the high-Z foils of converter, which scales with the energy as $\sim E^{-1}$. At high energy, on the other hand, the angular resolution is mostly dominated by the spatial resolution of the LAT Silicon Tracker. The transition between the two regimes occurs near a

[1] http://fermi.gsfc.nasa.gov/ssc/data/analysis/documentation/Cicerone/Cicerone_LAT_IRFs/IRF_EA.html

[2] https://www.slac.stanford.edu/exp/glast/groups/canda/lat_Performance.htm

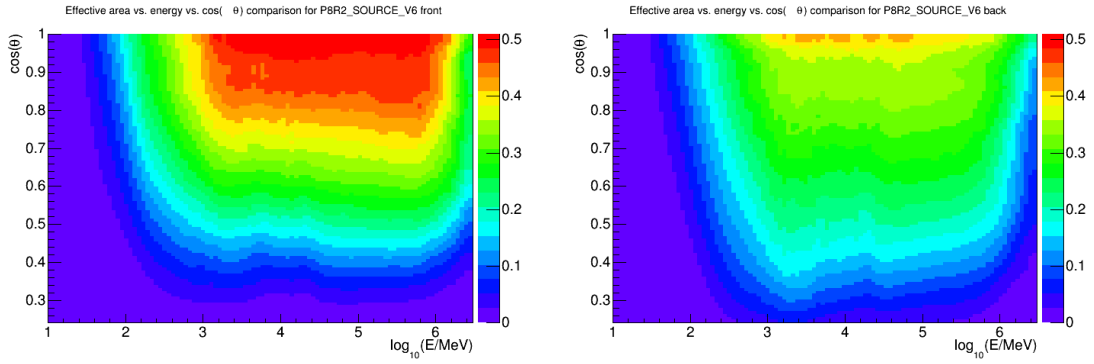

Figure 1.5: The effective area for Fermi LAT as described by the $P8R2\_V6$ IRF, `SOURCE` class, typical for the study of point-like sources; the lefthand column shows the effective area of the front section of the detector and the righthand column the back. The color scale is in units of m^2. Note the rapid change in efficiency with decreasing energy (and with increasing $cos\theta$). This has some impact on the energy binning chosen for generating exposure maps used in spectral analysis of the LAT data.[1]

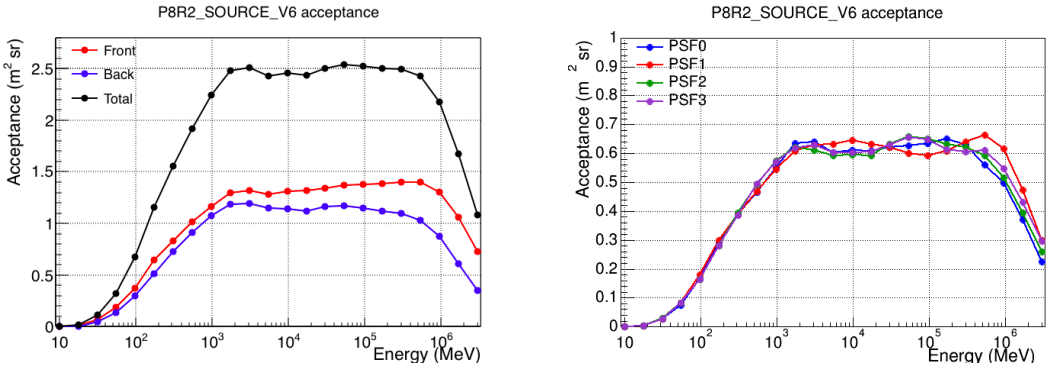

Figure 1.6: The acceptance of Fermi-LAT described by $P8R2\_V6$ IRF, `SOURCE` class, typical for the study of point-like sources; as a function of energy for all events (Total) and the FRONT/BACK, EDISP, and PSF event types.[2]

few GeV. The parametrization $S_P(E)$ describes the first order variation of the PSF with energy:

$$S_P(E) = \sqrt{\left[c_0 \cdot \left(\frac{E}{100\,MeV}\right)^{-\beta}\right]^2 + c_1^2} \tag{1.6}$$

Here, E is expressed in MeV, $\beta \sim 0.8$ and the other parameters (c_0 and c_1) varying across the LAT phase space.

Energy Dispersion

The Energy Dispersion, $D(E|E', \hat{p}')$, is the probability density to measure an event energy E for a γ-ray with $E', \hat{p}'$.
The energy dispersion is defined in terms of the fractional difference between the reconstructed (measured) energy E and the true energy E' of the events.

$$\frac{\delta E}{E'} = \frac{E - E'}{E'} \tag{1.7}$$

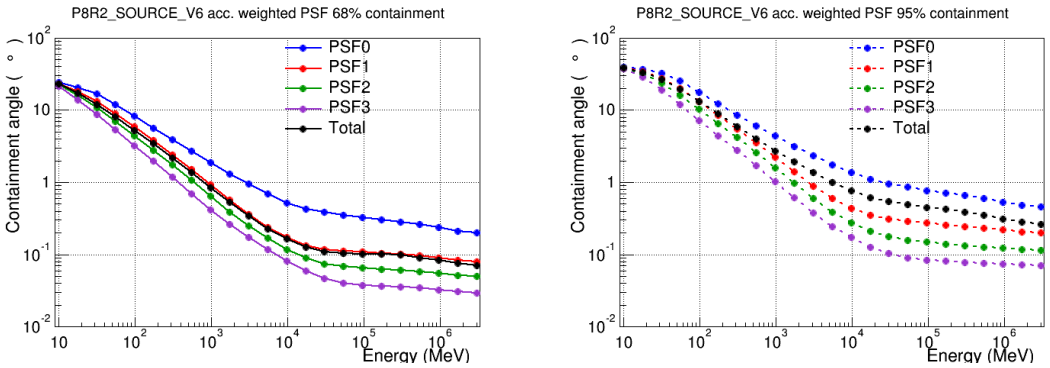

Figure 1.7: Containment angles at 68%(left) and 95%(right) of the acceptance weighted (acc. weighted) PSF for PSF event types of the characteristic $P8R2\_V6$ IRFs, `SOURCE` class, typical for the study of point-like sources (`https://www.slac.stanford.edu/exp/glast/groups/canda/lat_Performance.htm`).

For `Pass 8`, the energy resolution, defined i.e. as the minimum 68% containment interval of the energy dispersion, is $< 10\%$ between $1\,GeV$ and $100\,GeV$, which is sufficient to limit the spectral distortion to less than 5% in this energy range. Below $1\,GeV$ the energy measurement is more difficult and the energy resolution worsens: it is $\sim 20\%$ at $100\,MeV$ and $\sim 28\%$ at $30\,MeV$. As a consequence, ignoring energy dispersion when analysing data below $300\,MeV$ can induce potentially large systematic errors in the spectral fits of sources. While the energy dispersion correction reduces systematic uncertainties at all energies, the correction is particularly important below $100\,MeV$ where the induced fractional change in the counts spectrum can easily exceed the statistical uncertainties. Since we look at an γ-ray energy range between $10\,GeV - 1\,TeV$, we can ignore energy dispersion in our analysis.

As stressed previously, to evaluate the IRFs a dedicated Monte Carlo simulation is performed. A large number of γ-ray events are simulated in order to cover all possible photon inclination angles and energies with good statistics. This is based on the best available representation of the physics interactions, the instrument, and the on-board and ground processing to produce event classes (see Atwood et al., 2009 [16] and Ackerman et al., 2012 [5]).
However, the detection of a certain particle depends not only on the LAT hardware but also on the processing that calculates the event parameters from the observables and assigns probabilities that an event is a photon. The different event cuts are based on tradeoffs between the non-photon background, the effective area and the spatial and energy resolution. As a result the photon events are divided into classes, as we describe in the next section.
Moreover the IRFs performance parameters as all algorithms are optimized during the on orbit operations of Fermi. There are multiple IRFs delivered with the Fermi Science Tools to allow the user the flexibility necessary for the different analysis types, in our analysis we use the `Pass 8` release 2 version 6, known as `P8R2_V6`.
Figure 1.8 shows a comparison between different performance measures of the SOURCE class event in `Pass 8` and `Pass 7` (for the definition of SOURCE and other classes, see next section).

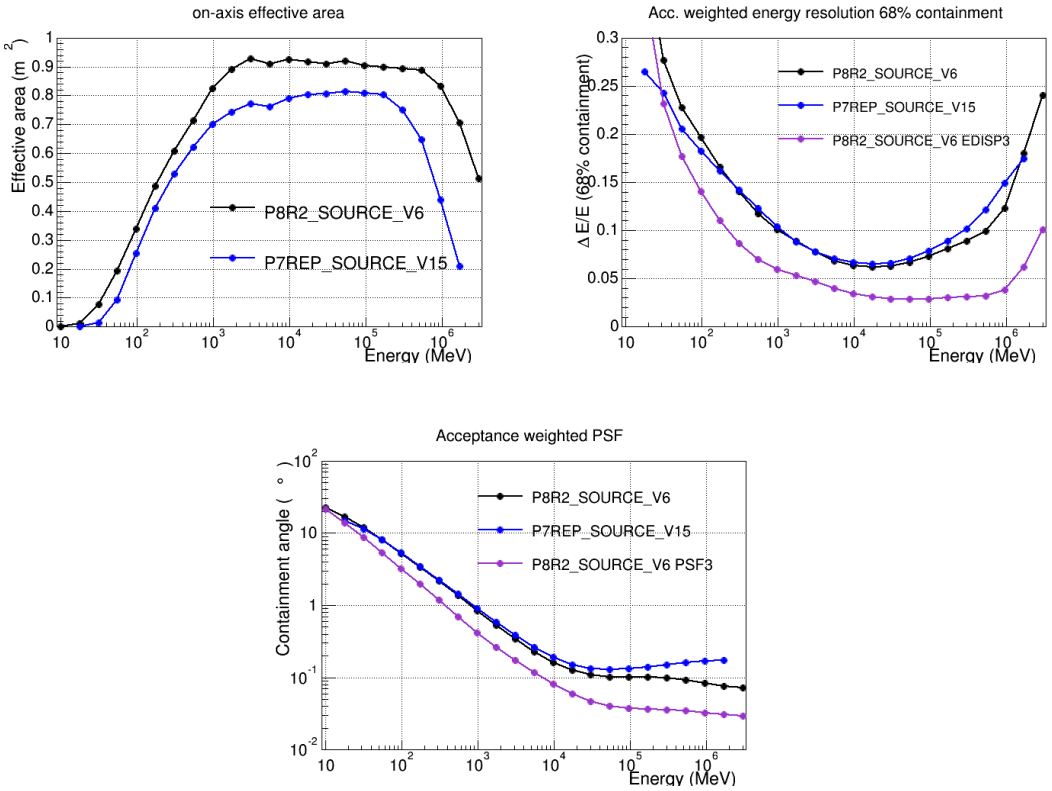

Figure 1.8: Comparison between `P7REP_SOURCE_V15` and `P8R2_SOURCE_V6` performance measures (`https://www.slac.stanford.edu/exp/glast/groups/canda/lat_Performance.htm`)

1.3.3 Background Rejection and Event Classification

The LAT instrument team makes cuts that classify the events based on their photon probability and the quality of their reconstruction. These cuts are used to separate events into event classes each of which is characterized by its own set of instrument response functions.

`Pass 8` has generated new event selection cuts that increase the acceptance over the entire LAT energy band, as a result it also corresponds to an increase in absolute background levels, but the signal-to-background ratios have been improved so that the point source sensitivity is improved over the whole LAT energy range. Thus it gives a more varied event classes classification respect the previous Passes released. As for the previous passes, it uses a Classification Trees (CTs) to select candidate γ-rays on the basis of the reconstruction outputs. The CT performance is evaluated from the combination of background rate and γ-ray acceptance that can be achieved for a given cut on the output signal probability. Background contamination in each class is calibrated to the best-fit power-law parametrization of the Isotropic Diffuse Gamma-Ray Background (IGRB) emission from Abdo et al., 2010 [1].

Each event class is composed of the following cuts: a selection on events with a reconstructed track that deposits at least $5\,MeV$ in the calorimeter, an ACD preselection on events for which the reconstructed track points to an activated section of the ACD, and an energy-dependent cut on CT variables for the particle type and the quality of the angular reconstruction.

Analysis classes differentiate by an increasingly tighter requirement that the candidate

photon events in both the tracker and the calorimeter behave as expected for γ-ray induced electromagnetic showers. Higher probability photon selections have smaller effective areas, narrower point spread functions (PSF), and lower contamination of background events. TRANSIENT classes have the loosest selection criteria are designed for short duration events, such as gamma-ray bursts, and timing studies that benefit from increased photon statistics while tolerating a higher background fraction and broader PSF. These classes have background fluxes that are generally equal to or greater than the IGRB. The other classes from SOURCE through ULTRACLEANVETO have a cleaner photon selections. These classes provide lower background contamination at the expense of lower effective areas, particularly at low energies, and have background fluxes that are generally equal to or lower than the IGRB. While SOURCE class is typically used for an intermediate selection, that is most favourable for analysis of moderately extended sources and point sources on medium to long timescales. ULTRACLEANVETO class have most restrictive selection, thus it is ideal for analysis of large regions that are more sensitive to spectral features caused by instrumental backgrounds.
Furthermore the event classes are organized in three nested hierarchies:

- **Standard hierarchy** contains all classes currently recommended for LAT analysis
- **Extended hierarchy** contains three TRANSIENT classes that are each supersets of the TRANSIENT classes in the Standard hierarchy (e.g. TRANSIENT020E is a superset of TRANSIENT020). They are defined with a less restrictive fiducial selection that accepts events with projected trajectories that do not pass through the Calorimeter. This selection improves the LAT effective area at low energies and high incidence angles ($< 100\,MeV$ and $\theta > 45\,deg$) but also slightly worsens the energy resolution.
- **No-ACD** classes are defined using selections that exclude variables associated with the Anti-Coincidence Detector and are therefore less susceptible to X-ray pile-up (ghost) activity which can occur during the impulsive phase of solar flares. However these classes generally have worse performance than the standard TRANSIENT selections when no pileup activity is present.

In Table 1.1 we give more detail about classes information, in particular their use in different type of analysis.
Then we have another classification with `Pass 8`, **event time** selection is a new scheme for partitioning data within an event class. These are essentially a generalization of **conversion type** (i.e., front vs back converting events). Each partition divides a class into independent subsets each with their own IRFs: effective area, point spread, and energy dispersion functions.
Three event type partitions are provided:

- **FB** Two event types for Front/Back conversion type. These are defined with the same selection on the tracker conversion plane as used in the Pass6 and Pass7 data releases.
- **PSF** Four event type quartiles for the quality of the PSF from PSF0 (worst) to PSF3 (best).
- **EDISP** Four event type quartiles for the quality of the energy reconstruction from EDISP0 (worst) to EDISP3 (best).

Event Class P8R2	Detail
	Standard Hierarchy
TRANSIENT020	Transient event selection with a differential background rate two times respect IGRB reference rate.
TRANSIENT010	Transient event selection with a differential background rate equal one times IGRB rate.
SOURCE	Source-like event selection with background rate less than the IGRB rate between $100\,MeV$ and $10\,GeV$ and ~ 2 times the IGRB rate above $10\,GeV$. This selection is primarily intended for point-source analysis and diffuse analysis at low galactic latitudes ($b < 30\,deg$). Relative to P7SOURCE this selection has a significantly lower residual background rate above $\sim 30\,GeV$.
CLEAN	Clean-like selection with a background rate less than the IGRB rate above $100\,MeV$. This selection is identical to P8SOURCE below $\sim 10\,GeV$. Above $10\,GeV$ this selection has a significantly lower background rate than P8SOURCE.
ULTRACLEAN	Ultraclean-like selection with a background rate that is less than P8CLEAN at all energies. It is intended for diffuse analyses which require a very low background contamination.
ULTRACLEANVETO	ULTRACLEAN selection with an additional cut that eliminates the non-isotropic background around $\sim 1\,GeV$ and also provides a further reduction in residual background at all energies. This class is provided for analyses which require a very low level of CR contamination and should be considered the preferred class for studies of the IGRB (diffuse emission).
	Extended Hierarchy
TRANSIENT020E	Transient event selection with a differential background rate equal to 2 times the IGRB rate, with a less restrictive fiducial cut on projected track length through the Calorimeter. This selection is a superset of $P8R2\_TRANSIENT020$.
TRANSIENT010E	Transient event selection with a differential background rate equal to 1 time the IGRB rate. This selection is a superset of $P8R2\_TRANSIENT010$.
	NON-ACD Hierarchy
TRANSIENT015S	Cleaner transient event selection intended for analysis of long timescale emission of solar flares. Differential background is roughly 1.5 times the IGRB rate.

Table 1.1: Detail of event classes classification.

For example, the Pass 8 SOURCE class selection can be partitioned in one of three ways: into front vs back converting events, into events belonging to one of 4 PSF subclasses, or into events belonging to one of 4 EDISP classes. We note that the PSF and EDISP event type selections were specifically optimized to partition the acceptance of SOURCE class.

Chapter 2

Fermi LAT observed Very High Energy (VHE) γ-ray Sources

The LAT large field of view in combination with its continuous all-sky coverage allows to have an almost uniform exposure of the sky every two complete orbits (about three hours), thus it is ideally suited to produce both general and specialized catalogs. Very High Energy (VHE) γ-ray sources, with energies $> 100\,GeV$, are extragalactic and galactic. The extragalactic Universe at these energies is dominated by Active Galactic Nuclei (AGNs), and in particular by strong variable source dubbed Blazars, a subclass of AGNs whose jet is aligned with the line of sight. In the extragalactic Universe an important role is played by transient sources like Gamma Ray Bursts (GRBs), that are shining flashes of radiation. The second group of Galactic sources consists of sources such as: Super Nova Remnants (SNRs), Pulsar Wind Nebula (PWNs) or binary systems (i.e. the so called microquasars).
When we observe the γ-ray sky, in addition to all these sources, we have to take into account the presence of a diffuse γ-ray emission given by the interactions of Galactic cosmic rays with gas and radiation fields; and a residual all-sky emission component, characterized by an isotropic distribution in the sky, usually referred to as the extragalactic γ-ray background (EGB). The EGB comprises all the contribution of thousands unresolved extragalactic sources, too faint or too diffuse to be resolved in a given survey, as well as any residual galactic foregrounds that are approximately isotropic, such as errors related to the detection system. Moreover, part of the this component may be related with the decay of exotic particles in the Primordial Universe. (Ajello et al., 2014 [11])
Both of them are also dubbed as Isotropic Diffuse Gamma-Ray Background (IGRB), thus the intensity attributed to the IGRB is instrument dependent because more sensitive telescopes are capable of extracting fainter sources.
We give a more detail description of Active Galactic Nuclei in section 2.3, since they are the dominated sources above $100\,GeV$. Thus now we focus on a general picture of all the other γ-ray sources, hinted above.

2.1 Gamma-ray Sources

2.1.1 Diffuse Emission

The diffuse emission dominates the entire γ-ray sky with the highest intensity coming from the plane of our Galaxy, as we can see in Figure 2.1. It can be explained through the energetic interactions between cosmic rays and the interstellar medium. Cosmic Rays (CRs) are very high-energy particles, composed primarily of protons,

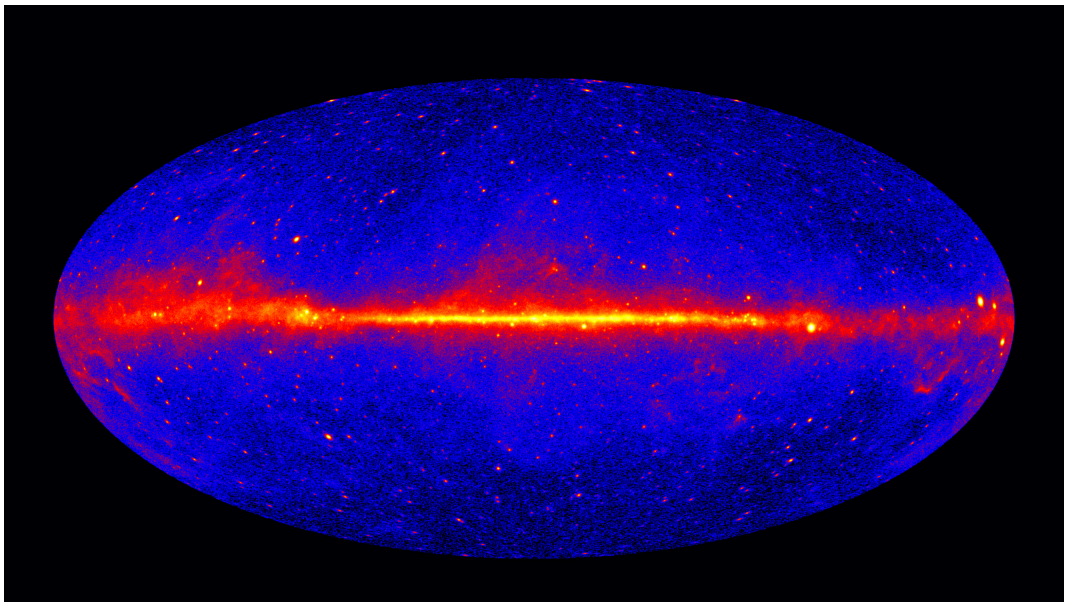

Figure 2.1: The Fermi LAT 60-month image, constructed from front-converting gamma rays with energies greater than $1\,GeV$. The most prominent feature is the bright band of diffuse glow along the map's centre, which marks the central plane of our Milky Way galaxy. The gamma rays are mostly produced when energetic particles accelerated in the shock waves of supernova remnants collide with gas atoms and even light between the stars. Hammer projection.[1]

atomic nuclei and leptons. Once they are accelerated up to relativistic velocities, through by not well known mechanisms, they move through the interstellar medium and they are trapped by the Galactic magnetic field. The diffuse γ-ray emission is then produced via

- Bremsstrahlung process, if a high-energy electron is deflected by nuclei of the interstellar medium (ISM)
- Inverse Compton (IC) process, if a high-energy electron transfers part of its energy to a soft photon coming from the stellar radiation
- π_0 decay, if a high-energy proton or atomic nucleus collides an interstellar proton creating a neutral pion

In all of these processes, the γ-ray production depends on both the cosmic ray energy density and the target density gas for Bremsstrahlung and radiation for IC scattering, leading to significant variations of the appearance of the HE sky as a function of energy, in particular when we look at the emission in our own Milky Way.
After removal of identified galactic point-like sources, the Galactic diffuse emission shows a structure that reflects the main features of the mass distribution in the Galaxy well known in all the wavelengths. The study of the diffuse emission gives information about spectra and intensities of cosmic rays species at distant locations and allows to study cosmic rays acceleration in Supernova Remnants (SNRs) and other sources and their propagation in the interstellar medium (ISM).

[1] `http://fermi.gsfc.nasa.gov/ssc/`

2.1.2 Extragalactic γ-ray background

The extragalactic diffuse γ-ray background is the summation of different contribution given by thousands of unresolved extragalactic sources, such as AGNs and a potential component due to the annihilation from exotic particles which originated from some unknown processes that took place in the primordial Universe. Moreover, there are hypotheses of its origin linked to particles deriving from extension of the Standard Model to supersymmetric particles (SUSY), which can contribute substantially to the Dark Matter content of the Universe and that can be found in the Galactic halos.

2.1.3 Galactic sources

As we point out we consider as galactic sources:

- the **Supernova Remnants** (SNRs) are the result of some of the most powerful explosions in the Universe, and they have great impact on their host galaxies, especially on their chemical enrichment and evolution. SNR shocks interact with the surrounding medium, heating and compressing it, as well as accelerating particles to relativistic energies. A modest efficiency of $\sim 10\%$ in converting the kinetic energy of supernova shocks into particle acceleration and the rate of SNRs in our Galaxy might explain the observed flux of cosmic rays. Hence, with the study of SNRs, a variety of astrophysical issues might be understood, such as the mass loss history of their progenitor stars, the nature of stellar collapse, and the mechanism behind the production of cosmic rays (CRs) from within our Galaxy.

- the **Pulsars** are rapidly-rotating neutron stars, i.e. the stellar remnant of a massive star ($M > 8M_{\odot}$) after its gravitational collapse, with a very intense dipole magnetic field, which emits a beam of detectable electromagnetic radiation with observed periods ranging from about $1\,ms$ to $10\,s$. The period is observed increase in time. We can observe the radiation when the beam of emission is pointing toward the Earth. From timing measurements, it is possible to estimate the strength of the magnetic field on the surface of the star, the age of the pulsar and other physical parameters.
  Pulsed emission represents only a little fraction of the total energy emitted by a pulsar. Most of the spin-down luminosity of energetic, young pulsars is carried away in a magnetized wind of charged particles. This wind expands into the surrounding medium, decelerating as it sweeps up ejecta from the supernova and forming a termination shock. These **Pulsar Wind Nebulae** (PWNe) contain both the relic accelerated particles from the pulsar and particles accelerated within the termination shock.

- the **Binary Systems**, in which very massive stars may collect the matter from stars in orbit around them. They have different characteristics and evolutions depending on the involved objects. X-ray binary systems are composed of a compact object, such as a neutron star or a black hole and a companion star (blue giant or white dwarf or very massive stars but less compact). In some binary systems, a central black hole produces relativistic jets and a companion is responsible for mass accretions. This class is also called *microquasar*, which comes from the observed morphological and physical similarities with quasars (a

class of AGNs). The mass of a microquasar is about seven orders of magnitude lower than that of a quasar. They are interesting because the processes taking place in AGNs can be studied in a shorter time in microquasars, considered from many aspects as their scaled-down versions.

2.1.4 Extragalactic sources

In addition to AGNs, that will be discussed in details later on, **Gamma Ray Bursts** (GRBs) are another kind of common extra-galactic sources. These are the most energetic and violent short term phenomena in the universe. These short bursts of radiation originate in galaxies out to the edge of the visible Universe (at redshifts of 0.03 to 9.4). The γ-ray emissions take place within very short time, from tens of milliseconds to few hundred seconds, in fact there are two observational varieties long-duration and short-duration GRBs, depending on the different types of progenitor stars. The first are due to the death of a rare type of massive star that produces a Type Ibc supernova with powerful relativistic jets. The latter are due to mergers of binary neutron stars, which create a central engine with highly collimated bipolar relativistic outflows of ejected material.
The *Fermi* LAT collaboration detected 111 GRBs, of this 73 GRBs are detected as sources[2].

2.2 Mechanisms of production of γ-rays

The search for sources emitting γ–rays is often analogous to the search for regions where high energy leptons or hadrons can be found; indeed are always produced by parent particles of higher energy. There are various different processes which lead to the production of γ-rays, which form characteristic spectral shapes. The main processes involving high energy γ-ray production are: synchrotron radiation, inverse Compton scattering, electron Brehmsstrahlung and pion decay, that now we briefly summarize.

2.2.1 Synchrotron Radiation

When a charged particle accelerates at relativistic velocity due to spiralling around a magnetic field, the electromagnetic energy emitted is called synchrotron radiation. Otherwise if the particle has a non-relativistic velocity the form is rather simple and is known as Cyclotron radiation.
In the relativistic case the particle is subject to effect of the Lorentz's force, the motion consists of two components: one is parallel to the lines of force, and the other is rotation around them at the angular frequency of Larmor precession. Due to the accelerated motion the radiation is emitted and it is beamed into a cone of angle $\theta \approx m_e c^2/E$ in the direction of the velocity, with an emission power:

$$P = \frac{2}{3} r_0^2 c B^2 \gamma^2 \beta^2 sin\phi^2 \tag{2.1}$$

where $r_0 = e^2/(m_e c^2)$ is the electron's classical radius, and ϕ is the angle between the velocity and B field vectors.
The critical frequency at which the maximum power is emitted is:

$$\nu_c = \frac{3}{2} \frac{\gamma^2 eBsin\phi}{m_e c} \tag{2.2}$$

[2]you can see the preliminary performed analysis in `http://fermi.gsfc.nasa.gov/ssc/observations/types/grbs/lat_grbs/table.php`

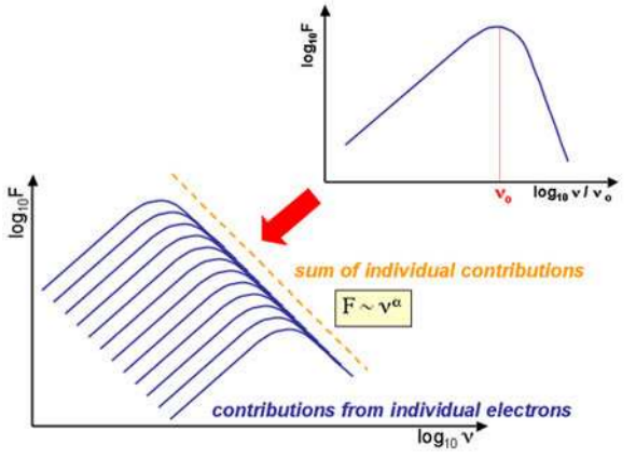

Figure 2.2: Synchrotron spectrum emitted in a typical astrophysical source.

Thus in a gas of relativistic electrons ($\gamma \gg 1$), a continuum spectrum is emitted. The power distribution follows an increasing power law, proportional to $\nu^{1/3}$, until it reaches a maximum, in correspondence to the maximum $\nu_m \approx 0.29\nu_c$. Above this maximum, it follows a decreasing exponential law, proportional to $\nu^{1/2}exp(-\nu/\nu_c)$. In astrophysical sources, usually electrons are not monochromatic, but their spectrum follows approximately a power law of index s. In such circumstances, the total power radiation distributes as well as a power law, of index $\alpha = (s-1)/2$.

2.2.2 Inverse Compton Scattering

Inverse Compton scattering involves the scattering of low energy photons to high energies by ultrarelativistic electrons so that the photons gain and the electrons lose energy. The process is called inverse because the electrons lose energy rather than the photons, the opposite of the standard Compton effect. The energy transfer to the electron therefore depends on the scattering angle of the photon. Maximum energy transfer occurs when the photon direction is reversed after collision, whilst minimum energy is transferred when the scattering angle is 90°. Since for low-energy collisions, the cross-section is simply the Thomson cross section $\sigma_T = \frac{8}{3}\pi r_e^2$, independent of energy. For very high energy electron-photon interactions, we have to consider the electron recoil, thus the Klein-Nishina cross-section is used, which at very high energies can be approximated (Longair, 1992) as:

$$\sigma_{KN} \simeq \pi r_e^2 \frac{m_e c^2}{x}(ln\, 2x + 0.5) \tag{2.3}$$

where $x = h\nu/m_e c^2$. If a population of energetic electrons with a power law distribution of index s interacts with a soft photons distribution of density ρ, the spectrum of γ–rays has the form $\propto E^{-(s+1)/2}$ and a typical characteristic energy of $\gamma^n\, h\nu$, where n = 1, 2 depending whether the regime is the Klein–Nishina or Thompson one, and γ is the electron Lorentz factor.
This process could be particularly important for the production of high energy γ–rays in relativistic jets.

2.2.3 Bremsstrahlung

Charged particles in a gas are deviated by electromagnetic interactions with other particles, such as nuclei or ions, and emit a radiation known as Bremsstrahlung or free–free radiation. Bremsstrahlung photons generated by cosmic-ray electrons will have a power-law spectral distribution similar to the energy distribution of the electrons.
Bremsstrahlung by thermalized electrons, also known as thermal Bremsstrahlung, is the most important emission mechanism in cold ionized plasma, such as the intracluster medium (typical temperature of 10^7 K, emission in the X–ray domain of the spectrum), or the accretion disk in AGNs. The electrons, in this case, have a mean velocity related to the temperature of the plasma: $v \simeq (k_B T)/m_e$. The emitted spectrum is flat for frequencies smaller than $(2\pi k_B T)/h$, and fall rapidly above this threshold.

2.2.4 Pion decay

Gamma rays can also be generated as a result of proton interactions. A very common interaction in high-energy astrophysical systems is the collision of cosmic-ray protons with stationary hydrogen gas. The neutral pion π_0 provide the main channel of conversion of the kinetic energy of protons into high energy γ-rays. The lifetime of neutral pions is very short ($\tau = 8.410^{-17}\, s$), and their decay produces two gamma rays. However, neutral pions are rarely created at rest, and since they suffer no energy loss by ionisation, they usually decay in flight. TeV gamma rays can be produced by neutral pions travelling at relativistic speeds. The decay of pions is also important for the development of hadronic cosmic-ray showers in the atmosphere.

2.3 Active Galactic Nuclei (AGNs)

Active Galactic Nuclei (AGNs) are the most luminous sources of electromagnetic radiation that covers all the electromagnetic spectrum. They are compact objects located at the center of galaxies and produce a higher luminosity than the host galaxies in a very concentrated volume. Active galaxies show partly non-thermal spectra, concentrated in the very centre of the galaxies, now thought to be due to matter in an accretion disc falling into a super-massive black hole (SMBH) of $10^6 - 10^{10} M_\odot$ mass (Lynden Bell, 1969 [40]).
Because AGN are so luminous, they can be observed out to very high redshifts. As we say this makes them excellent probes of the early Universe, i.e if we observed a source (AGN) at redshift $z = 6$ this corresponds to a look-back time of almost 95% of its age, and should further our understanding of the evolution of the Universe as a whole.
The intergalactic medium can also be well studied, by looking at the absorption lines in the spectra of distant quasars, as can gravitational lensing effects. The huge masses of the central black holes, and the corresponding extreme gravitational fields, allow the investigation of General Relativity; for example some AGN show very broad, skewed iron line profiles in their X-ray spectra, suggesting that they are formed close to a spinning black hole (Wilms et al., 2001 [59]).

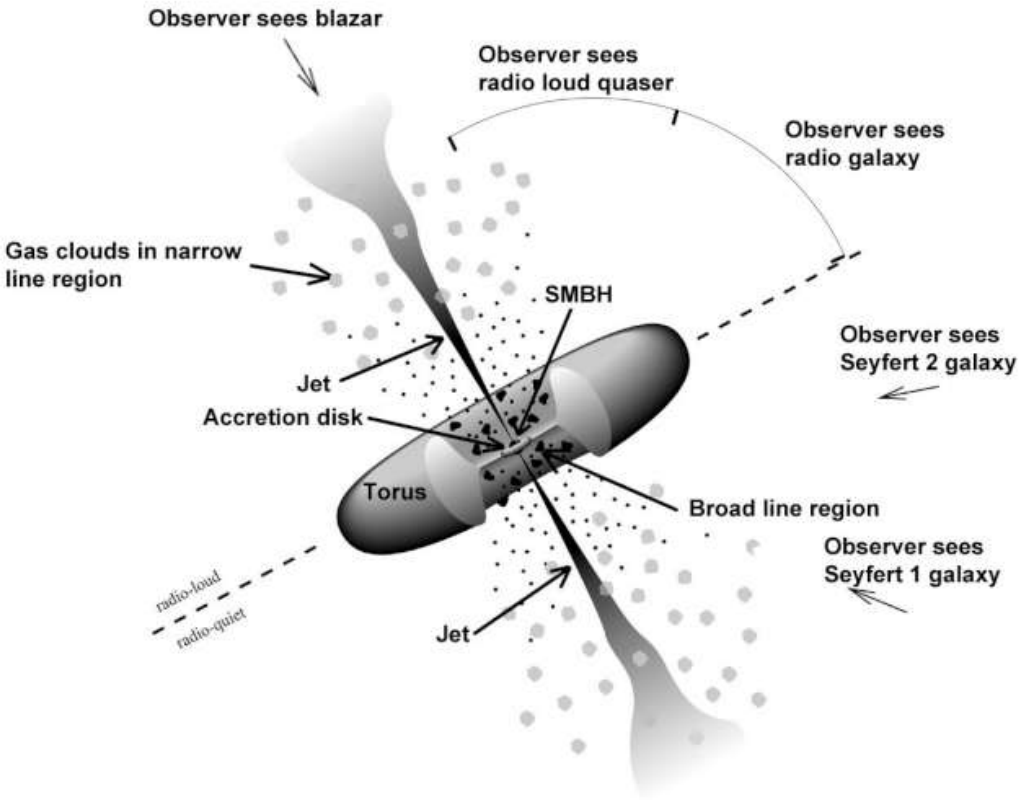

Figure 2.3: Graphic representation of an AGN with only one jet, as described by the modern Unifying Theory. As can be seen in this basilar schema AGNs are divided on the viewing angle on which they are observed and on the radio-loudness of the source. For radio-loud objects, which are in the upper part, there is another subdivision in classes FR-I and FR-II, whose dividing line is populated by the BLAZAR's family composed by BL Lacs and Flat Spectrum Radio Quasars (FSRQs).

2.3.1 Structure

The most accreditate model that describes the AGN structure is presented in Figure 2.3.
At the center of the host galaxy there is a *supermassive black hole* (SMBH), with $10^6 - 10^{10} M_\odot$ mass, whose gravitational potential energy is the source of AGN radiation. Cold material, close to the central black hole, is attracted by the black hole gravity, spirals in and coalesce into an *accretion disk*. Through dissipative process in the accretion disk, matter is transported inwards and angular momentum outwards, causing the accretion disk to heat up and emitting radiation. A *corona* of hot material forms above the accretion disc and can inverse-Compton scatter photons up to X-ray energies. A fraction of this ionizing radiation (of the disk) excites clouds of gas moving around the deep potential well of the black hole. Through photoionization and collisional excitation processes they generate strong emission lines in the optical and ultraviolet. Clouds region at a distance of $10^{17} - 10^{18}\, cm$ (less than a parsec) from the black hole generates emission lines broaden by Doppler shift, this is why this region is called *Broad Line Region* (BLR). At greater distance, about $100\, pc$, less dense clouds are moving less rapidly than the previous region, and they show lines with a narrow width. Therefore this region is called *Narrow Line Region* (NLR). Moving away, at several parsecs from the black hole, there is a geometrically thick structure made of interstellar gas and dust, called *torus*, that intercepted a large fraction of the AGN's radiation and re–emits it in the infrared. It was empirically deduced by evidence about spectral observation.
Some of these AGNs accelerate relativistic bipolar jets of ejected material to relativistic speeds, which stretch up to hundreds of kiloparsecs outside the host galaxies. Their direction likely traces the rotational axis of a spinning black hole. Therefore the jet emission is highly beamed, and their appearance depends on the viewing angle.

2.3.2 The Black Hole paradigm

For a long time it has been argued about how AGNs can generate such a huge amount of energy in such a small region. Accretion can potentially give very efficient conversion of potential and kinetic energy to radiation.
Supermassive black holes are now believed to exist in the centres of most if not all massive galaxies since the mass of the black hole correlates well with the velocity dispersion of the galactic bulge (the M-sigma relation) or with bulge luminosity. Thus AGN-like characteristics are expected whenever a supply of material for accretion comes within the sphere of influence of the central black hole.
As mentioned, matter tends to form an accretion disc around objects such as black holes, so that its initial angular momentum can be dispersed, via viscous drag: assuming the system is Keplerian, differential rotation will occur, with the material closest to the black hole moving more quickly than the distant matter. This causes the particles to move inward towards the centre of the gravitational field. As the particles fall inward, angular momentum is transferred outward through the accretion disc. As well as causing the inward movement of material, viscous drag dissipates heat, increasing the temperature of the accretion disc. Matter falling toward a massive object releases energy according to

$$L = \eta \dot{M} c^2 \tag{2.4}$$

where L is the source luminosity, $\dot{M} = dM/dt$ is the mass accretion rate onto the black hole, η is the efficiency of the process and c is the speed of light. Typical

AGNs efficiency is $\eta \sim 0.1$, an order of magnitude more efficient than the fusion of Hydrogen to Helium in stars, for which $\eta = 0.007$, and it is within a factor of ten of annihilation energy mc^2.
Such an object would be supported in hydrostatic equilibrium, by balancing the gravitational force acting on an electron-proton pair by a central mass M: $\vec{F_g} = -(GMm_p/r^2)\hat{r}$, where we neglect the electron mass, respect the proton mass, with the radiation force on protons and electrons in an optically thin plasma. The force per electron is just the rate at which momentum is deposited per unit time, so we multiply by $p = E/c$, the photon momentum to obtain

$$\vec{F}_{rad} = \left(\frac{L\sigma_T}{4\pi r^2 c}\right)\hat{r} \tag{2.5}$$

Here, we assume a steady, spherically-symmetric accretion and take ionized hydrogen as accreting material, thus the photons-matter interactions can be treated as a simple Thomson scattering and σ_T is the Thomson cross section.
Since $\vec{F_g}$ and $\vec{F}_{rad}$ both scale as $1/r^2$, there is a critical luminosity, the Eddington limit, above which radiation pressure exceeds gravity:

$$L_{edd} = \frac{4\pi GMm_p c}{\sigma_T} \simeq 1.26 \times 10^{-38} \frac{M}{M_\odot}\, ergs\, s^{-1} \tag{2.6}$$

To ensure efficiency through the accretion mechanism, then the total luminosity cannot overcome the Eddington luminosity.

2.3.3 AGNs Classification

Previously we have described that the presence of the torus obscures the direct observation of the nucleus, therefore AGN appearances and properties vary considerably with the observing angle formed by the relativistic jets with the direction from which the active nucleus is observed, as we can see in Figure 2.3.
The Unified Model, as we see in Table 2.1, classifies AGNs according to their radio loudness and their optical spectra. (Urry & Padovani, 1995 [56])
Radio loudness classifies AGNs in radio-loud and radio-quiet objects. The former ones have emission contributions from both the jet(s) and the lobes that the jets inflate. These emission contributions dominate the luminosity of the AGN at radio wavelengths and possibly at some or all other wavelengths. The latter ones are simpler, since jet and any jet-related emission can be neglected at all wavelengths.
Optical spectral classifications AGNs in Type 2, 1, 0. Whether they have narrow emission lines, we are looking straight on the plane of the torus, we have a Type 2. If they have only broad lines, the line of sight does not intercept the torus, we have Type 1. At last if they present weak or unusual emission lines, when their jets are orientated very close to the observer's line of sight, they are called Type 0.

Type 2 (Narrow line): these AGNs present weak continua and only narrow emission lines. This implies that high velocity gas cannot be observed, which maybe due to the presence of a thick wall of absorbing material blocking our view.
Radio-quiet include at low luminosities: Seyfert 2 galaxies, and the narrow-emission-line X-ray galaxies. The high-luminosity candidates are the infrared-luminous IRAS AGN, which may show a predominance of Type 2 optical spectra.
Radio-loud group, also called Narrow-Line Radio Galaxies (NLRG), include two different morphological types: the low-luminosity Fanaroff-Riley type I radio galaxies,

which have often-symmetric radio jets whose intensity falls away from the nucleus, and the high-luminosity Fanaroff-Riley type II radio galaxies, which have more highly collimated jets leading to well-defined lobes with prominent hot spots.

Type 1 (Broad line): these AGNs have bright continua and broad emission lines, from hot, high-velocity gas located deep in the gravitational well of the central super massive black hole.
The radio-quiet group include: the Seyfert 1 radio galaxies and radio-quiet quasars (QSO). The first have relatively low luminosities and therefore are seen only nearby, while the latter have higher-luminosity and they are typically seen at greater distances.
The radio-loud include: Broad-Line Radio Galaxies (BLRG) at low luminosities and radio-loud quasars at high luminosities, either Steep Spectrum Radio Quasars (SSRQ) or Flat Spectrum Radio Quasars (FSRQ) depending on radio continuum shape.

Type 0 (Unusual): these galaxies have very unusual spectral characteristics. Their spectra either lack strong absorption or emission features, or they present them but with very unusual traits. They are characterised by rapid variability at optical wavelengths.
A small fraction of radio-quiet AGN are know as BAL (Broad Absorption Line) quasars, in fact they show broad absorption features in their optical and ultraviolet spectra.
Radio-loud objects as BL Lac and Flat Spectrum Radio Quasars (FSRQ) are called Blazars. The first (BL Lac) objects are characterized by very rapid variability, high and variable polarization, high brightness temperatures, superluminal velocities of compact radio cores and at last they have a spectrum more bluer than FSRQs. With bluer we means that the peak frequencies of both peaks are higher. While at low luminosities both energy humps have the same power, then the higher one increases its relevance as we increase the luminosity. (bolometric) In fact the most powerful FSRQ have an high energy hump that is 10 times greater than the low energy one.

AGN		**Type2** (Narrow Line)	**Type1** (Broad Line)	**Type0** (unusual spectra)
Black Hole	Radio Quiet	Seyfert 2 QS0	Seyfert 1	
Spin ? $\Downarrow$	Radio Loud	NLRG { FR I, FR II }	BLRG { $SSRQ$, $FSRQ$ }	Blazar { $BL\,Lacs$, $FSRQ$ }
		decreasing angle to the line of sigh $\Rightarrow$		

Table 2.1: AGN classification based on both the radio-loudness and the optical properties of the sources.

2.3.4 Blazars, a subclass of AGNs

Blazars are the most extreme class of AGNs known. Basically, blazars are AGNs observed face-on, with the jet pointing toward the observer. They emit energies at all wavelengths, showing a strong continuum emission from radio to Very High Energy (VHE) γ-rays. Indeed they show a high polarization, at both optical and radio frequencies, and rapid variability at all frequencies and on all time scales. The Spectral Energy Distribution (SED) of blazars is dominated by the non-thermal continuum produced within the jet and boosted by relativistic effects (Urry and Padovani, 1995 [56]). According to the presence or absence of strong broad emission lines in their optical/UV spectrum, blazars are traditionally divided into flat-spectrum radio quasars (FSRQs) and BL Lacertae (BL Lacs) respectively.
Therefore it displays two broad peaks, a low-energy component from radio through UV or X-rays, and a high-energy component from X-rays to γ-rays up to above $1\,TeV$. Widely interpreted as due to Synchrotron (low frequency peak) and Inverse Compton (high frequency peak) mechanisms.
Blazars, defined by the location of the peak of the low-energy Synchrotron SED component, are also sub-divided into several types:

- Low Synchrotron Peaked (LSP), consisting of FSRQs and Low Frequeny Peaked BL Lac Objects (LBLs), having synchrotron peak in the IR regime, at $\nu_s \leq 10^{14}\,Hz$;
- Intermediate Synchrotron Peaked (ISP), where Intermediate BL Lac Objects (IBLs) are found, have their synchrotron peak at optical-UV frequencies in the range $10^{14}\,Hz < \nu_s < 10^{15}\,Hz$;
- High-Synchrotron-Peaked (HSP), almost all known to be High Frequeny Peaked BL Lac Object (HBL), are synchrotron peaked at X-ray energies with frequencies $\nu_s > 10^{15}\,Hz$.

FSRQs are almost all LSP blazars, while BL Lacs on the other hand are equally divided into LISP (LSP+ISP). This subdivision leads to what is referred to as blazar sequence. (Fossati et al, 1998 [26])
As shown in Fig.2.4 two peaks are present in all the SEDs. The first one, due to synchrotron emission, is anticorrelated with the source luminosity, and it is moving from $\sim 10^{16}$–$10^{17}\,Hz$ for less luminous sources to $\sim 10^{13}$–$10^{14}\,Hz$ for the most luminous ones. The X-ray spectrum becomes harder while the γ-ray one softens with increasing luminosity, indicating that the second (Compton) peak of the SEDs also moves to lower frequencies from $\sim 10^{24}$–$10^{25}\,Hz$ for less luminous sources to $\sim 10^{21}$–$10^{22}\,Hz$ for the most luminous ones.
Therefore, the frequencies of the two peaks are correlated: the smaller the $\nu_{peak,sync}$, the smaller the peak frequency of the high energy component. Increasing L_{5GHz} increases the γ-ray dominance, which is the ratio of the power emitted in the IC and synchrotron components, estimated with the ratio of their respective peak luminosities.

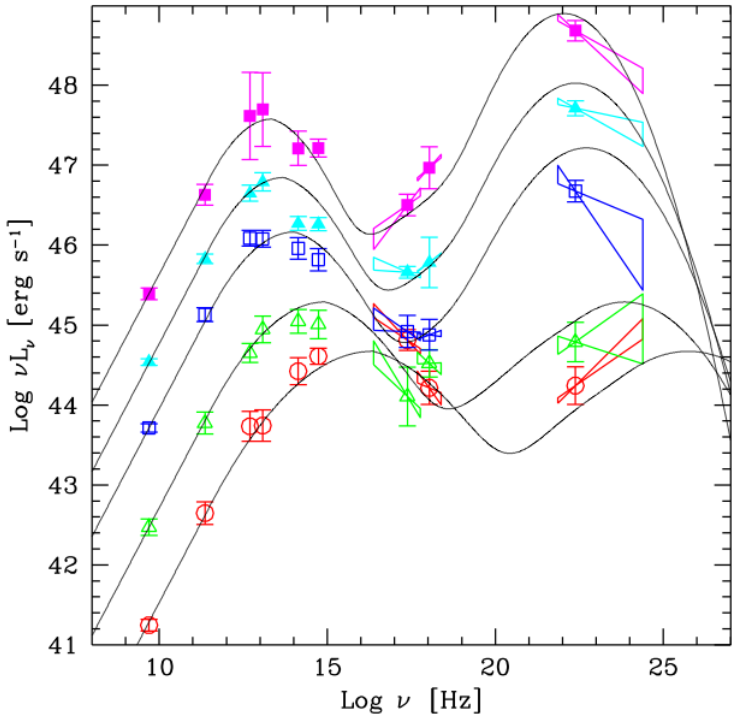

Figure 2.4: The blazar sequence concept of Fossati et al., 1998 [26]. The peaks on the left hand are the Synchrotron peaks, starting from LSPs objects located on top down to HSPs at the bottom as the frequency ν increases. On the other hand, the peak in the right hand are high energy Inverse Compton peaks, visibly correlated to the other ones.

2.4 Catalogs of γ-ray Sources

The knowledge of γ-ray sources before the launch of the *Fermi* came mainly from the experience of the EGRET telescope on board the Compton Gamma-ray Observatory (CGRO) in particular from the results of the Third EGRET Catalog (Hartman et al., 1999 [32]). The Third EGRET Catalog consists of 271 sources: 5 pulsars, 1 solar flare, 66 high-confidence blazar identifications, 27 possible blazar identifications, 1 likely radio galaxy (Cen A), 1 normal galaxy (LMC), and 170 unidentified sources. A sixth EGRET pulsar is shown in the figure for completeness (at l=69, b=3), but is seen only in pulsed data, and so is not included in the catalog. Since 2000, several authors revisited the data of EGRET instrument because of the new discoveries in the field of γ-ray astronomy. One of the main results of this re-analysis was the production of a new catalog after a modified diffuse background subtraction (Casandjian & Grenier, 2008 [23]).

Thanks to Fermi, we get an energy range that guarantees the exploration of the energy range between the EGRET upper limit and the lower limit of the ground based telescopes, a spectral window that could contain a lot of new high energy sources.

Fermi team releases several catalogs, among them, the latest ones and more useful in our analysis, are: the second catalog of hard Fermi-LAT sources (2FHL) and third Fermi Large Area Telescope source catalog (3FGL). In addition to new sources identified, each catalog includes a number of improvements in the analysis as advancements in calibration level reconstructions of events, an updated model Diffuse Emission of Galactic and new methods to associate the sources of LAT to potential counterparts at other frequencies.

The Fermi 3FGL catalog (Acero et al., 2015 [4]) is the result of four years of observation data in $100\,MeV$–$300\,GeV$ energy range by the *Fermi* LAT. It implemented a number of analysis refinements respect to the previous Fermi released catalog: LAT Bright Source List (0FGL, Abdo et al. 2009d), the First Fermi LAT (1FGL, Abdo et al. 2010d), and the Second Fermi LAT (2FGL, Nolan et al. 2012); of which it is the successor. The analysis improvement has been done thanks to:

- Pass 7 reprocessed data, the principal difference relative to the original Pass 7 data used for 2FGL is improved angular resolution above 3 GeV
- a new model of the diffuse Galactic and isotropic emissions. It allows to have a higher likelihood in source detection, especially for regions where the diffuse emission cannot be described using a spatial template and the accuracy of the model is improved toward bright star-forming regions and at energies above $40\,GeV$
- taken into account the finite sizes of the sources allows for more accurate flux and spectrum measurements for the extended sources as well as for nearby point sources
- a refine method for characterizing and localizing source seeds evaluated, that gives most marked improvements at low Galactic latitudes.

Table 2.2 shows the population distribution of the types of sources detected by the Fermi LAT. It includes 3033 sources above 4σ significance. As we can see, unassociated sources comprise 33.29% of the catalog, followed by BL Lac type blazars.
With the new event-level analysis called Pass 8 (see 1.3 at pg. 14), that increases significantly the sensitivity of the LAT resulting in an acceptance improvement at least of 100% below 100 MeV and about 25% above 1 GeV, the Fermi Collaboration prepared the second catalog of hard Fermi-LAT sources (2FHL). The 2FHL catalog is based in 80 months of Pass 8 data photons with reconstructed energy in the $50\,GeV - 2\,TeV$ range. The γ-ray sky shines at this energies with approximately 61000 photons, which in turn led to the detection of 360 sources. The 2FHL catalog contains, at $|b| < 10°$, 70% of sources associated to BL Lac population, 23% are uncertain blazar type (BCU) and unassociated sources and only 7% are associated to other source populations, 4% of them are FSRQs. Due to their characteristics, the frequency of the synchrotron peak and the photon index, almost all BCU and unassociated sources are expected to be BL Lacs therefore the fraction of blazars in the 2FHL catalog is about 97% (93% BL Lacs and 4% FSRQs). (Ackermann et al., 2015, [7]).

Source Type	Number	Percentage of 3FGL
Non-Blazar Active Galaxy	3	0.10%
Active Galaxy of Uncertain Type	573	18.89%
Binary	1	0.03%
BL Lac Blazar	660	21.75%
Compact Steep Spectrum Quasar	1	0.003%
Flat Spectrum Radio-Loud Quasar	484	15.95%
Normal galaxy	3	0.10%
Globular Cluster	15	0.49%
High-Mass Binary	3	0.10%
Narrow-Line Seyfert 1	5	0.16%
Nova	1	0.03%
Pulsar[1]	143	4.71%
Pulsar[2]	24	0.79%
Pulsar Wind Nebula	12	0.40%
Radio Galaxy	15	0.49%
Starburst Galaxy	4	0.13%
Seyfert Galaxy	1	0.03%
Star-Forming Region	1	0.03%
Supernova Remnant	23	0.76%
Special Case[3]	49	1.62%
Soft Spectrum Radio Quasar	3	0.10%
Unassociated	1010	33.29%
Total	3033	

Table 2.2: 3FGL catalog sources. The population of sources in 3FGL is dominantly unassociated, followed by BL Lac blazars (Acero et al., 2015 [4]).

[1] Identified by pulsations; [2] No pulsations seen by LAT;

[3] Potential association with supernova remnant or pulsar wind nebula.

Source Type	Associated Designator	Number
Pulsar	psr	1
Pulsar wind nebula	pwn	14
Supernova Remnant	snr	16
Supernova remnant/Pulsar wind nebula	ssp	4
High-mass binary	hmb	2
Binary	bin	1
Star-forming region	sfr	1
BL Lac type of blazar	bll	180
BL Lac type of blazar with prominent galaxy emission	bll-g	13
FSRQ type of blazar	fsrq	10
Non-blazar active galaxy	agn	2
Radio galaxy	rdg	4
Radio galaxy / BL Lac	rdg/bll	2
Blazar candidate of uncertain type I	bcu I	7
Blazar candidate of uncertain type II	bcu II	34
Blazar candidate of uncertain type III	bcu III	19
Normal galaxy (or part)	gal	1
Galaxy cluster	galclu	1
Total associated		312
Unassociated		48
Total		360

Table 2.3: 2FHL catalog sources (Ackermann M. et al., 2015 2.3).

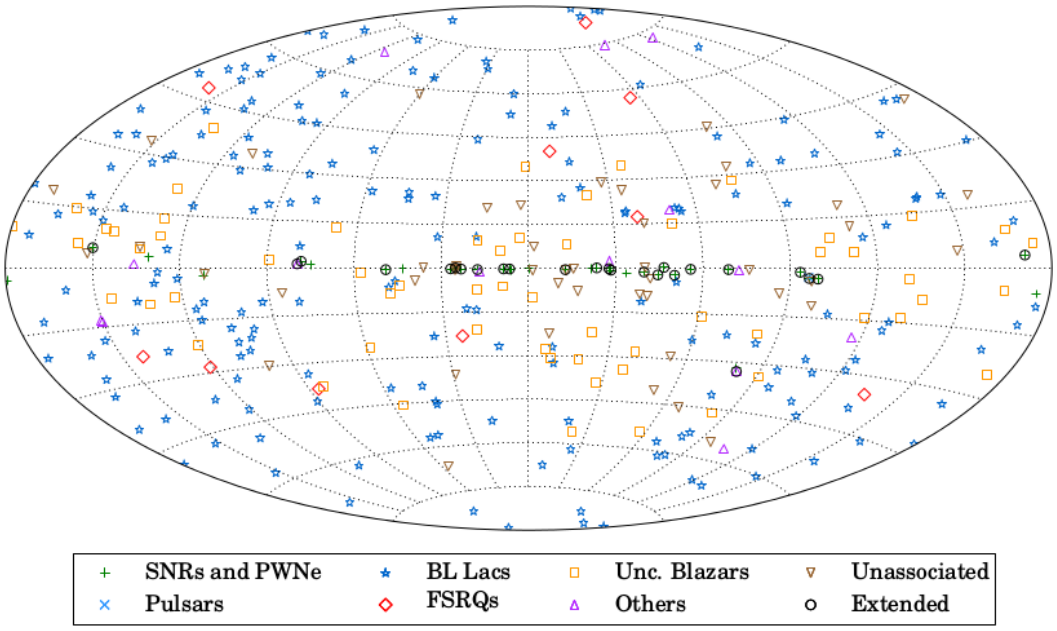

Figure 2.5: Sky map, in Galactic coordinates and Hammer-Aitoff projection, showing the sources in the 2FHL catalog classified by their most likely association. (Ackermann et al., 2015 [7])

Chapter 3

Data Analysis

Almost all the files that are input to, or output from, the Science Tools are FITS files. FITS stands for "Flexible Image Transport System" and consists of a sequence of Header Data Units (HDUs). The first HDU is likely to contain information about the instrument(s) or the history of the data; subsequent HDUs consist of binary formatted tables/matrices of data or images. The Fermi-LAT Science *Tools* provide the basic software necessary for the analysis of data from the Fermi-LAT; the online documentation is supported by the Fermi Science Support Center (FSSC)[1].
From the Fermi web server, one may obtain processed data files corresponding to the data acquired by the LAT over a given time range, energy range, coordinate ranges. An FT1 file, also known as an **Event file**, contains the data for each gamma ray event, such as Right Ascension, Declination, Energy, Zenith Angle, Time, Event Class, etc.
Two types of events files are provided with different event class pre-selections called: *Photon Data* and *Extended Data*. While the first contains all information necessary for science analysis with `SOURCE`, `CLEAN`, `ULTRACLEAN`, or `ULTRACLEANVETO` event classes; the latter contains all event data, including the standard Transient classes (`TRANSIENT010` and `TRANSIENT020`), plus additional parametres with respect to the Photon Data.
An FT2 file, also known as a **Spacecraft file**, contains observation start and stop times, and the following variables for 30 seconds intervals: positions, McIlwain parameters (used in the description of the geomagnetic field), SAA flag, LAT mode, and livetime.
Preparing these data for the analysis depends on the kind of the source one wishes to analyse, e.g.: point source, extended source, GRB spectral analysis, timing analysis, etc. The different cuts to the data are described in detail in Cicerone.[2]

3.1 Data Selection

The analysis performed in this work concentrates on data collected by the LAT from October 29th 2008 to January 11th 2016 with the `Pass8` and the current IRFs released version `P8R2_V6`. Since one of the main aim is to point out new sources and, in particular we are interested in a point-source analysis, we selected the `SOURCE` class (see Table 1.1 for complete details). The selected energy range is between $10\,GeV$ and $1\,TeV$.

[1] `http://fermi.gsfc.nasa.gov/ssc/`

[2] `http://fermi.gsfc.nasa.gov/ssc/data/analysis/documentation/Cicerone/Cicerone_Data_Exploration/Data_preparation.html`

We point out that we do not take into account the LAT data collected in the time period between August 4th and October 29th 2008, since there is an anomaly in the data probably due to a problem in the acquisition, as it seems that too much noise was accepted as viable data. In fact the time distribution of this collected photons does not follow the expected Poisson distribution and, accordingly, the interval of time elapsed between two consecutive events does not follow an exponential distribution. (see Milotti, 2014 [46])
We downloaded the primary FT1 file data from the Fermi LAT Astro Data Portal Server.[3]

Cut name	Value
Science Tools version	11-00-00
Instrument Response function	P8R2_SOURCE_V6
E_{min}	10 GeV
E_{max}	1 TeV
T_{start} (MET)	247000129
T_{end} (MET)	474175306
Zenith	90°
Evclass	SOURCE
ABS(ROCK_ANGLE)	$< 52°$

Table 3.1: Selection criteria for the data to which the clustering analysis was applied.

3.2 C and Python Scripts

For this analysis we wrote some C scripts in order to compute the clustering analysis that find clusters. We use C scripts because they are much faster with respect to an analogue analysis done with a Python scripts, thus they are more suitable when we compute a huge amount of data, as the all data time analysis. On the other hand, we wrote some Python scripts in order to use the *Fermi Tools*, in this case they are more suitable. In particular we use a Python script to apply the time cuts on the entire data set as well as to perform the maximum likelihood analysis.
We performed the followed steps:

3.2.1 Clustering Algorithm

We use *ClustDistance.c*, a C script, in order to build clusters from an input file of photons. For each photon contained in the input file fits it associates a cluster. Thus we obtain a number of clusters equal to the input number of photons.
Clusters are computed as follows:

- we calculate for each i-photon, the cluster's i-center, the angular distance with respect to all other j-photons, $ang\_dist(i_{ph,center} - j_{photon})$
- a j-photon is eligible to be in a cluster if the angular distance from the i-center is less than the sum of containment angle at 95% of the characteristic Point Spread Function of each photon:

$$ang\_dist(i_{ph,center} - j_{photon}) < ca95\_i_{ph,center} + ca95\_j_{photon} \tag{3.1}$$

[3] `http://glast-ground.slac.stanford.edu/DataPortalAstroServer/?tab=Astro%20Server`

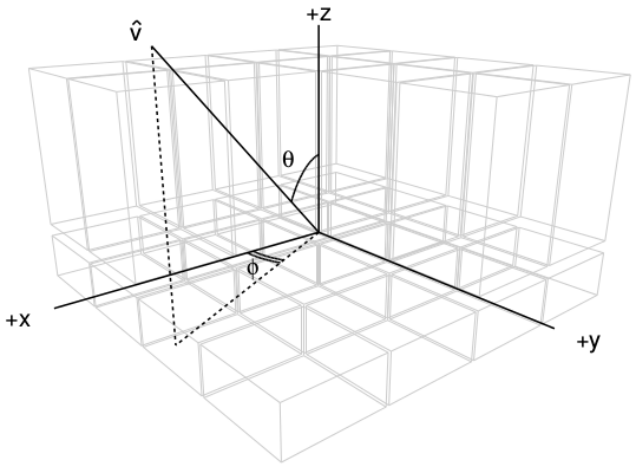

Figure 3.1: This figure defines the (θ, ϕ) coordinate system used. Where θ is the angle of incidence of the event with respect to the LAT boresight (+Z axis of the spacecraft) and ϕ is angle of incidence of the event with respect to the +X axis. It represents a schematic of the LAT, including the layout of the 16 CAL modules and 12 of the 16 TKR modules (from Ackermann et al., 2012 [5])

- each cluster is characterized by a list of the following parameter: the i-photon center and its characteristic classification type (i.e. if it is a psf0, psf1, psf2, psf3), the mean direction (RA, DEC), the photons number within the cluster and the radius.

PSFs Containment Angle at 95%

Our first analysis step is to obtain the containment angle at 95% for different PSF event types. This is one of the main parameter used in order to build the clustering algorithm.
We know that each photon-event is characterised by PSF event type parameters and its typical quartiles, that indicate the quality of the reconstructed direction; through PSF0, the worst quartile in the quality of the reconstructed direction, to PSF3, the best quartile in the quality of the reconstructed direction.
Thus we wrote a Python script[4] that for a given quartile at a given energy E, θ and ϕ, return the PSF containment radius at 95%. See Figure 3.1 for definition of the chosen coordinates.
As we look at the Figure 1.7(on the left), that we enlarged here in Figure 3.2, the containment angle at 95% does not show much energy dependence, above $10\,GeV$.
However, it shows a strong dependence on θ, the reconstructed angle of incidence of the event respect to the LAT bore-sight (the zenith of the spacecraft - the line normal to the top surface of the LAT directed away from Earth), as a results PSF event types depend on θ reconstructed angle.
We can explain this behaviour if we recall both the effective area definition (see pg. 18 Eq. 1.3) and the event PSF. In both cases we assume that ϕ, the reconstructed angle of incidence of the event with respect to the x axis (the line normal to the sun-facing side of the spacecraft), is not important. The dependence of the effective area on ϕ for the analyses, integrated over long, or even moderate, time intervals on the exposure on 12 hour time scales is $< 3\%$ RMS at all energies.

[4] `/afs/slac.stanford.edu/u/gl/denisec/script/ca95.irf/psf.py`

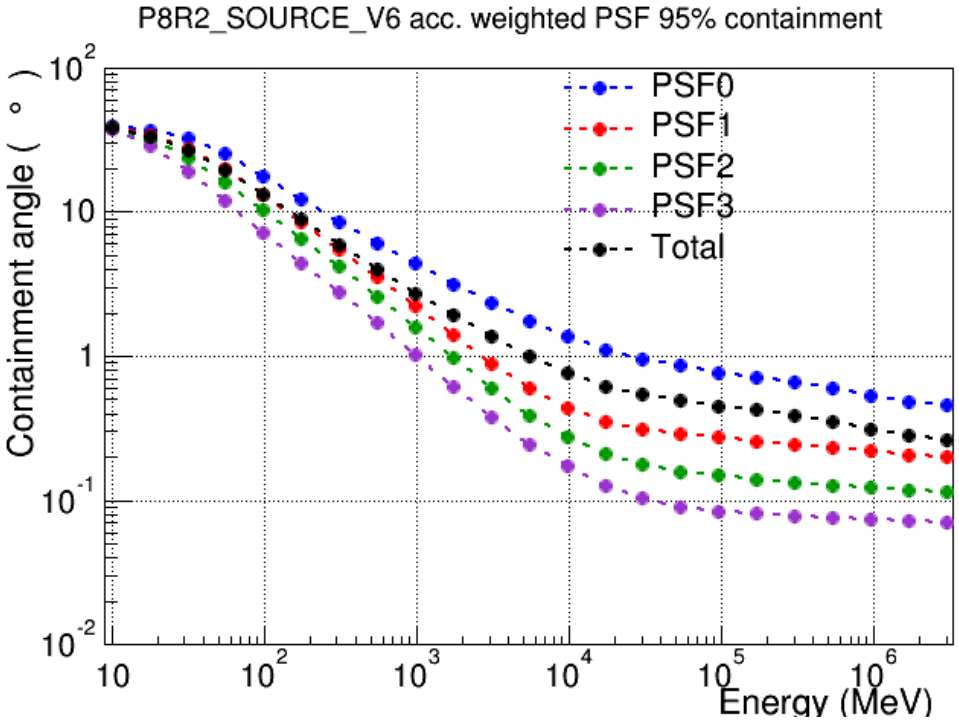

Figure 3.2: Containment angles at 95% of the acceptance weighted (acc. weighted) PSF for PSF event types of the characteristic $P8R2\_V6$ IRFs, `SOURCE` class. We point out that the containment angle at 95% in the energy range in which we are interested, above $10\,GeV$, does not show a strong dependence on energy.

This also holds for the PSF: the variations of the containment radii with ϕ are many times smaller than the corresponding variations with θ for all but the highest energies $\lesssim 100\,GeV$.
We can see in Figure 3.3 the θ dependence of the effective area for photons with a fixed energy of $10\,GeV$ and for different quartiles of PSF event type. As the incidence angle increases, the fraction of particles the LAT is capable of register progressively decreases for a combination of geometrical factors (for example because they miss the CAL or the TKR) and the elevate difficulty of reconstruct correctly such events.
We highlight the θ dependence by using the definition of the PSF. The PSF is the probability density dP to observe an event in a small portion of solid angle $d\Omega$ centred on Ω given that event originated from Ω_0. That is, for a given energy (that we suppress here) and incidence angle, the PSF is

$$\frac{dP(\Omega)}{d\Omega} = \frac{dP(\Omega)}{d\phi\, dcos\theta} \approx \frac{1}{2\pi}\frac{dP(cos\theta)}{dcos\theta} \approx \frac{1}{\pi}\frac{dP(\theta^2)}{d\theta^2} \tag{3.2}$$

where ϕ is the azimuthal angle and θ the polar angle measured respect the origin Ω_0, and where we have made the approximations of azimuthal symmetry and small angular deviations. We see that the natural variable is θ^2, the squared angular deviation, as isotropic sources ($dP/d\Omega$ constant) are flat in this quantity. As a result we define $u \equiv \theta^2/2\sigma^2$ variable, in terms of which Eq. 3.2 becomes:

$$\frac{dP(\Omega)}{d\Omega} \approx \frac{1}{2\pi\sigma^2}\frac{dP(u)}{du} \tag{3.3}$$

Indeed in order to describe the power-law behavior of the PSF at large angular offsets the functional form adopted by the LAT team is the King function (King, 1962 [37]).

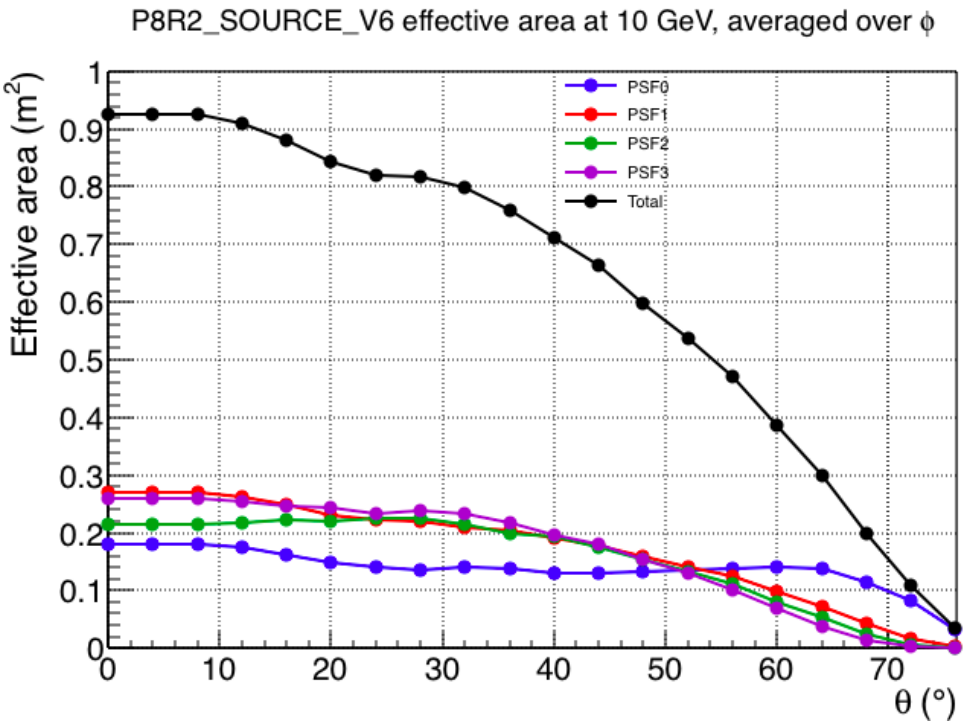

Figure 3.3: The effective area for Fermi LAT as described by the $P8R2\_V6$ IRF, `SOURCE` class; as a function of incidence angle theta for 10 GeV photons.

The King function has the form

$$K(x,\sigma,\gamma) = \frac{1}{2\pi\sigma^2}\left(1-\frac{1}{\gamma}\right)\left(1+\frac{x^2}{2\sigma^2\gamma}\right)^{-\gamma} \tag{3.4}$$

Here, $x = \delta/S_P(E)$ is the scaled angular deviation, since $S_P(E)$ is the scaling function that parametrized the PSF energy dependence, defined in Eq. 1.6 on pg. 19.
K is normalized in the small-angle approximation $d\Omega = x\,dx\,d\phi$, so that

$$\int_0^{2\pi}\int_0^{\infty} K(x,\sigma,\gamma)xdxd\phi = 1 \tag{3.5}$$

The parameter σ is the characteristic size of the angular distribution and γ determines the weight of the tails of the distribution. The King function becomes the normal distribution in the limit $\gamma \to \infty$, where $1.51\sigma \approx 68\%$ containment.
In reality a single King function fit is not enough to properly reproduce the observed distributions of simulated γ-rays. As described in Ackermann et al. [6] a more complex model is given by the sum of two King functions

$$P(x,E) = f_{core}K(x,\sigma_{core}(E),\gamma_{core}(E)) + (1-f_{core})K(x,\sigma_{tail}(E),\gamma_{tail}(E)) \tag{3.6}$$

where the *core* and *tail* components characterize the distributions for small and large angular separations, respectively. The parameters γ_{core} and γ_{tail} determine the structure of the PSF tail and are found from simulations to decrease at high energy, yielding larger tail fractions above $\approx 10\,GeV$.

Therefore the cuts on theta values we performed for different PSF quartiles are widely justified by the above consideration. In addition, for every PSF type, we can

PSF quartile	cut on theta (deg)
0	70
1	70
2	68
3	68

Table 3.2: Cut on theta values that we choose for different PSF quartiles.

compute the containment angle at 95% (hereafter CA95), in particular the CA95 maximum value we obtain from photons of $10\,GeV$: 1.4° for PSF0 photon type, 0.45° for PSF1 photon type, 0.3° for PSF2 photon type, and at least 0.2° for PSF3 photon type. Just as we highlighted previously the PSF3 photon type is the best quartile reconstruction, as a matter of fact it has a smaller value than the other. Looking at Figure 3.4, that represent the calculated CA95 of a fixed PSF quartile (or type) in function of θ inclination angle, we make a proper cut on theta for each PSF quartile in other to obtain the expected CA95 value range. We summary the cuts made in Table 3.2.

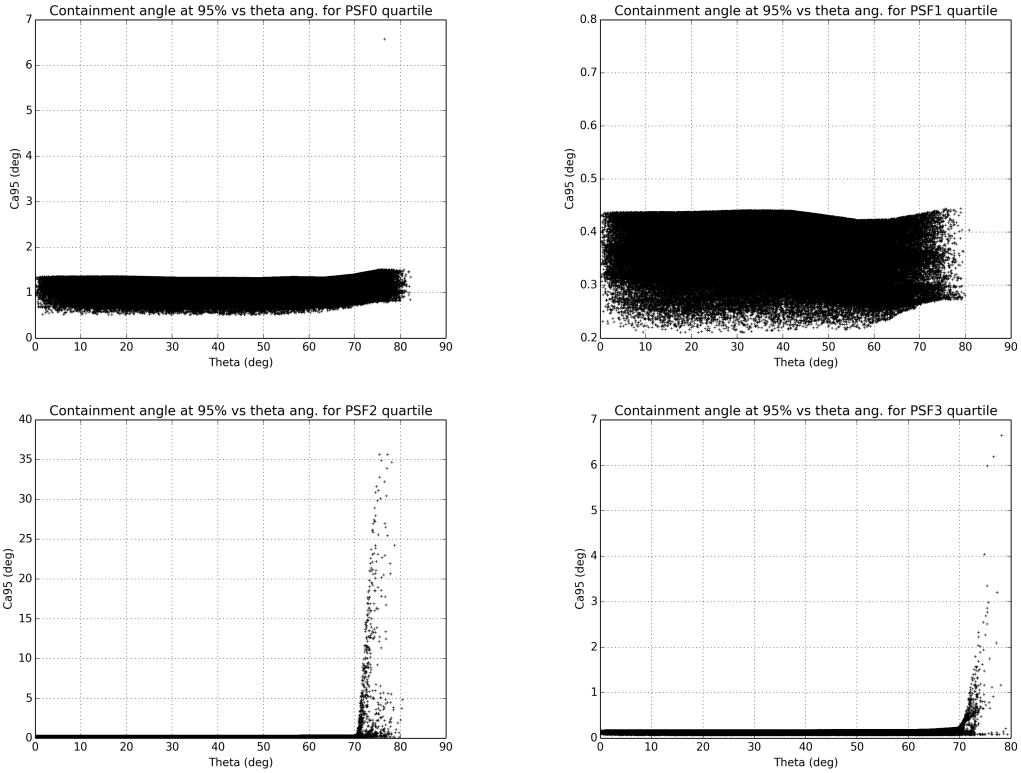

Figure 3.4: Containment angle at 95% of a fixed PSF quartile in function of θ inclination angle. From the top we show the photons of PSF0 type (on the right), PSF1 type (on the left). From the bottom respectively photons of PSF2 (on the right) and PSF3 type (on the left).

The Radius

We define the radius of the cluster as an estimator of its dispersion. We choose empirically a definite radius for each cluster as the second tercile, or rather about the 66%, of the distance from the i-center photon, from which the cluster begins to be computed, and the last photon belonging to the cluster. A small radius indicates that photons that meet the angular distance condition 3.1 tend to be close to the cluster's mean position. Otherwise a large radius indicates that photons are spread out over a wider range of distances, thus we suppose we have an higher probability that this type of cluster contains photons that come from the Isotropic Diffuse Gamma-Ray Background (IGRB) and are not emitted from a source.

3.2.2 Clusters' Merging

The next step we have to perform is merging clusters. We have to delete clusters that contain a certain percentage or all the same photons. As we highlighted in 3.2.1 paragraph we obtain a number of clusters equal to the input number of photons. This step is simple if we analyse a restricted data sample, one where we analyse only photons contained in small time intervals. In fact, if we look at data sample of few days, for example one or two day samples, a cluster associate with a known or unknown source, is repeated for N times, equal to the contained photons number, in the same sky position and with the same photons number. Thus we have only to take one of this repeated clusters and delete the other.
However, when we extend the time intervals to 30 days of collected or even the whole data set, we have a stronger contribution from the Isotropic Diffuse Gamma-Ray Background and, as a result, clusters around the same point source change their position and the number of contained photons.
At first we applied an angular distance requirement analogous to the one used for the photons (in Equation 3.1). If the angular distance condition of a j-cluster respect to another i-cluster is less than the sum of they respective radius, the two clusters overlap. We suppose that the more numerous cluster, in terms of contained photons are more suitable to be associate with a source, so we delete the less numerous one. This procedure is repeated for each cluster, that belongs to the list of clusters created by the previous step.
It does not seem to be a good choice in case we have sources that are near one another, for example the known catalogue sources which lie in the galactic plane, because we risk that the more numerous cluster with a greater radius emerge at the expense of less numerous one.
As Harel D. and Koren, 2001 [31] explained, this is a typical negative point of partitional clustering algorithms, the class of algorithm to which our analysis belong. Indeed we obtain a single partition of the data that optimizes a certain criterion, minimizing the overall squared distance between each data point and the center of its related cluster. This tends to work well with isolated and compact clusters.

All data set analysis

The list of clusters, obtained after this step, is strongly dependent on the type (PSF0, PSF1, PSF2, PSF3) of the photon used as starting seed. If we allow photons of all PSF types to be cluster seeds then we get as clusters list only clusters that have a PSF0 photon type as seeds, as PSF0 is quite larger than the other ones.
We can understood this behaviour if we look at Figure 3.5 that represents clusters numerosity and radius in function of clusters' different seed types. Due to their

greater PSF containment angle at 95%, PSF0 photon type respect to the other photon type named PSF1, PSF2, PSF3 have greater radius and, accordingly, a greater numerosity. Therefore a single cluster (with PSF0 as a seed) has a greater probability to have photons in common with other clusters. Eventually, most clusters overlap, making our algorithm barely usable.

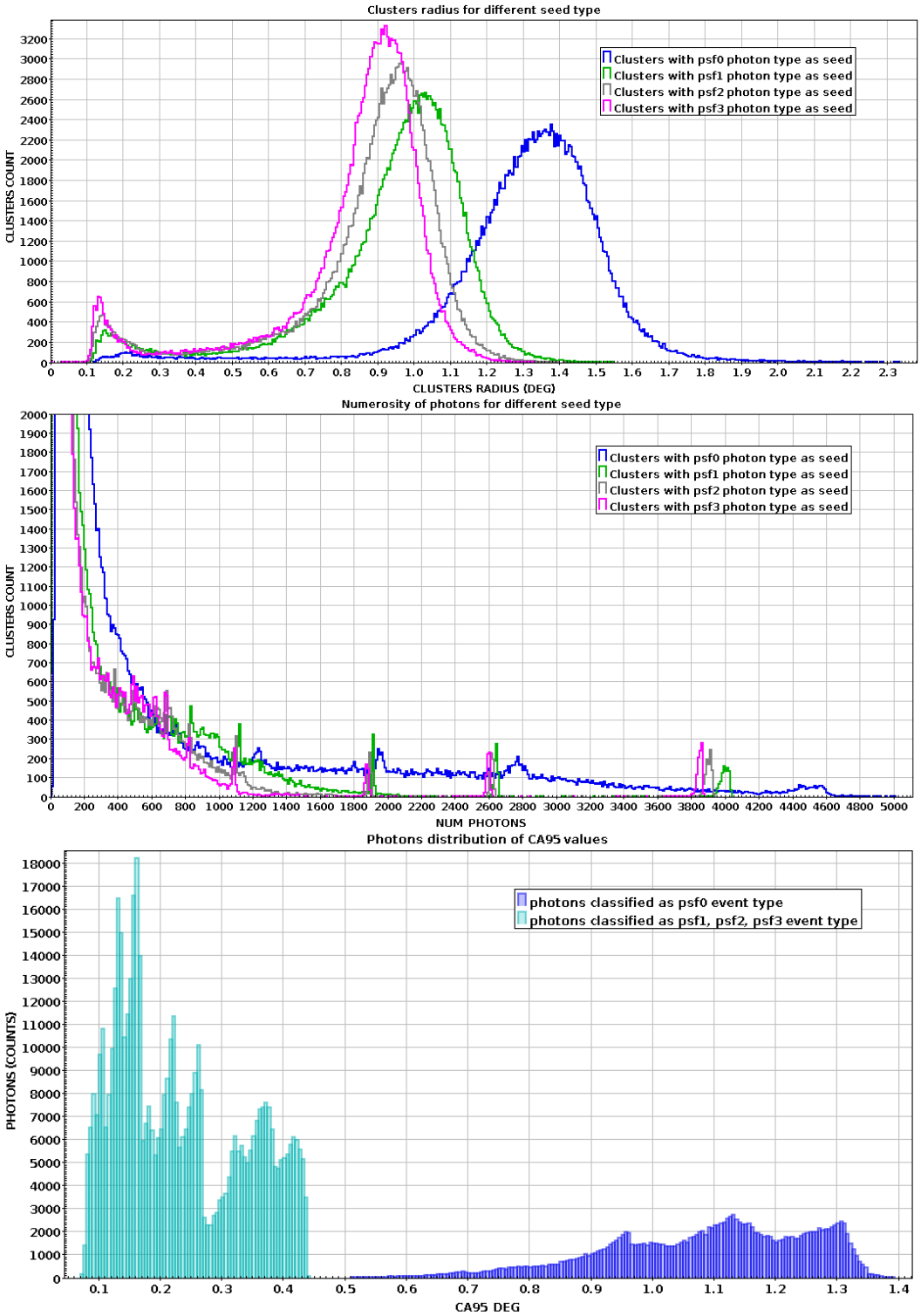

Figure 3.5: On the top histograms of clusters radius, on the middle the numerosity, in terms of photons within the cluster radius, both of them in function of different photon type of seed. The blue, green, grey and magenta curve represents the clusters radius(on the top) or numerosity(on the bottom) respectively of clusters with a photon type psf0, psf1, psf2 or psf3 as a seed. Like we expected the more numerous and the greater radius clusters are with a psf0 photon type as a seed. We note two different behaviour of the clusters radius distribution. While the green, grey and magenta curves show a double peak, the blue one shows a single peak at a radius of 1.37°. This is a result of the different distribution of CA95 values for different photons types classification. The bottom graphs shows the CA95 distribution of photons. While CA95 values of photon type classified as psf1, psf2, psf3 behave in the same way and follow the light blue distribution. CA95 values of photon type classified as a psf0 have a different distribution, the blue one.

3.2.3 Time Sliding Window

Our aims are both to identify new sources, better detectable in larger time intervals, as well as detecting flaring activities by known sources, typically diluted and hidden in larger time interval analysis since their signal-to-noise will be too low. Therefore we analyse the whole *Fermi* LAT data set (about 7 years) as well as study shorter-time interval datasets. We use a Python script[5] in order to performed cuts on time value. We choose to analyse different time data sets as 30 days, or specific time data set of one-two days. The latter one aimed at checking if our algorithm is able to point out specific flares already detcted by the *Fermi* LAT Collaboration, thus we check how confident we are in pointing out sources.

3.3 Clustering Issue

During our analysis we encountered an issue, as you can see in Figure 3.6, that represents the clusters distribution in galactic coordinate (l, b), there is an ecliptic anomaly of numerous clusters in terms of photon contained (which contains a numbers of photons between 100-200, the blue points, and between 50-100, the green one) with galactic longitude value between $\sim [90° - 160°]$ (with a longitude radius between $[15° - 20°]$).
This anomaly is fictitious, in fact it is due to a bad approximation of the angular distance calculation. At the beginning, we calculated the angular distance using the spherical law of cosines, known also as Bessel formula, that is quite fast, in order to reduce the computational time of the algorithm. However, the spherical law of cosines formula can have large, relative, rounding errors if distances are small, as in our case. Therefore, we used a more complicated formula that is accurate for all distances, a special case of the Vincenty formula for an ellipsoid with equal major and minor axes. The angular distance with the Vincenty formula may be comouted as:

$$\delta = \frac{|v_1 \times v_2|}{v_1 \cdot v_2} \tag{3.7}$$

where v_1 and v_2 are vector in spherical coordinate.
None of the same, the computational error helped us to highlight a different exposition of the *Fermi* LAT telescope toward the North and South Celestial Pole, see Figure 3.7, where the photon disttibution is biased toward North by roughly 10%.

[5] /afs/slac.stanford.edu/u/gl/denisec/script/pythonScript/fcopyCut.py

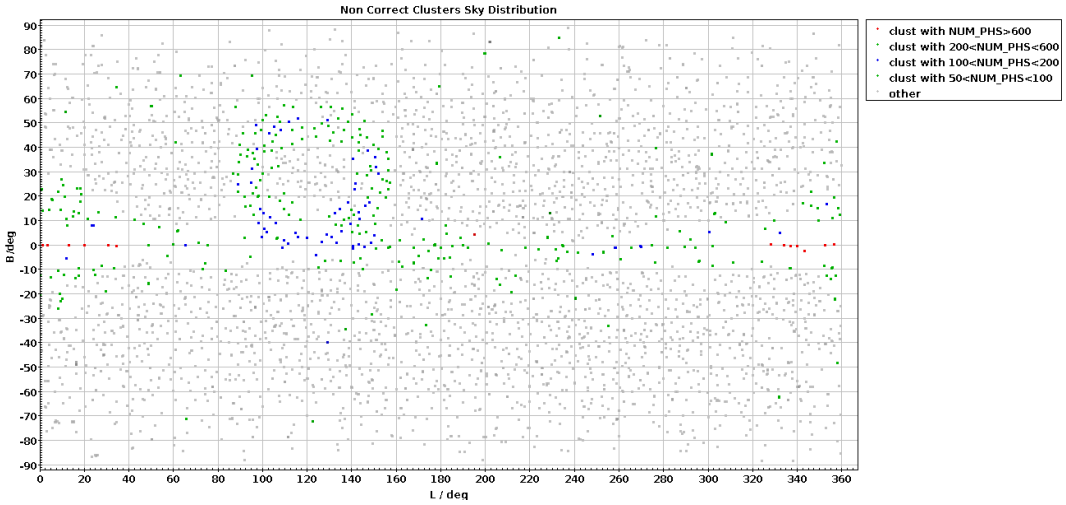

Figure 3.6: Clusters Distribution in Galactic cooordinate (L,B) shows an accumulation of numerous clusters, in terms of content photons, about 100phs (blue points) and 50phs (green points) for each cluster, in a certain sky region. This region shows an ecliptic form, with galactic longitude value included between $\sim [90° - 160°]$.

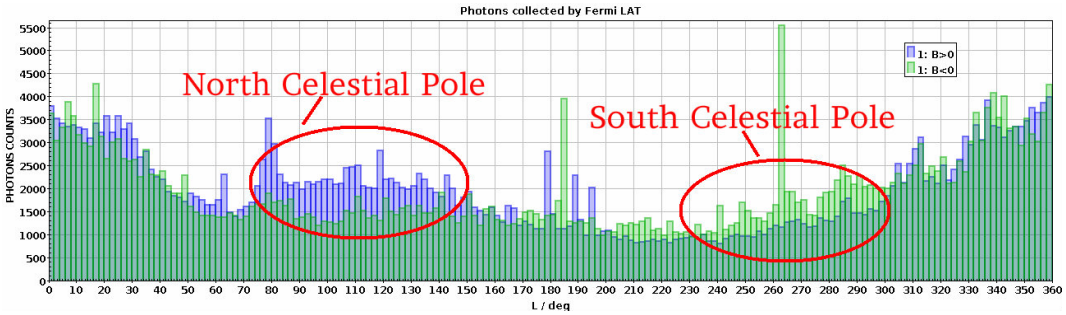

Figure 3.7: Histogram of photons galactic longitude collected by *Fermi* LAT, the blue one represents photons with galactic latitude B greater than 0 ($B > 0$), while the green one photons with galactic latitude B less than 0($B < 0$). The difference of collected photons between the two highlighted circles that represents the North and South Celestial Pole is about 10%.

3.4 Maximum Likelihood Analysis of LAT Data

After obtaining the list of clusters we use a Maximum Likelihood Approach in order to evaluate if a cluster could be associated with a new source. Using the Unbinned Likelihood Analysis we analyse each cluster position. This is the preferred method for time series analysis of the LAT data, where the number of events in each time bin is expected to be small. Otherwise, for large time bins, which includes bright background sources (such as the Galactic plane), and long time-baseline spectral and spatial analyses, it is more suited a binned analysis.

3.4.1 Likelihood analysis for photon-counting experiments

Photon counting telescope experiments, such as COS-B (Pollock et al., 1981, 1985 [51]), EGRET (Mattox et al., 1996 [43]), and *Fermi* LAT use the method of maximum likelihood (Neyman and Pearson, 1928 [47]) to analyse data. The maximum likelihood framework has proven generally useful in the context of gamma-ray astronomy, and

is currently the standard statistical approach for high level LAT data analysis tasks such as determining the spectral shapes of γ-ray sources. Let us assume to have a model describing the observations supposed to be known except for a finite number of parameters. Let $M(E', \hat{p}', t; \lambda_k)$ be the differential flux per unit area at the detector predicted by the model as a function of true photon energy E', true photon arrival direction at the detector $\hat{p}'$, time t and of the unknown parameters $\{\lambda_k\}_{k=1,\ldots,m}$. Thus recalling the IRFs definition (at 1.3.2) the expected count rate J in the instrument phase space is given by the convolution of the source differential flux per unit area at the detector with the IRFs:

$$J(E, \hat{p}, t; \{\lambda_k\}) = \int dE' d\hat{p}' \, R(E, \hat{p}|E', \hat{p}', t) M(E', \hat{p}', t; \{\lambda_k\}) \tag{3.8}$$

The counts expected in a given energy range (E_1, E_2) , solid angle Ω and time interval (t_1, t_2) are then obtained as the integral of the differential count rate in the detector.

$$\Lambda(\{\lambda_k\}) = \int_{t_1}^{t_2} dt \int_{\Omega} d\hat{p} \int_{E_1}^{E_2} dE \, J(E, \hat{p}, t; \{\lambda_k\}) \tag{3.9}$$

LAT events are typically binned in three dimensions: two *spatial* dimensions (with two coordinates we identify a direction o, equivalently, we operate in the real projective space RP^3) and energy. We can label each spatial pixel in each energy bin by an index, i. The observed number of counts in each bin is characterized by the Poisson distribution:

$$f(n, \nu) = \frac{\nu^n}{n!} e^{-\nu} \tag{3.10}$$

where ν is the number of expected counts from the model in each bin of observing n counts.
The likelihood is defined as the product of Poisson probabilities (for each pixel i) for finding the observed counts N_i, given the model expected counts $\Lambda_i\{\lambda_k\}$.

$$\mathscr{L}(\{\lambda_k\}) = \prod_i f(N_i, \Lambda_i\{\lambda_k\}) \tag{3.11}$$

For large data sets, the likelihood is likely to be a very small number. Since the logarithm of monotonic functions is again monotonic, we can instead maximize the "log likelihood", which is also often easier to compute. (or rather the maximum of the likelihood $\mathscr{L}$ corresponds to the minimum of $-\log \mathscr{L}$)

$$\begin{aligned} \log \mathscr{L}(\{\lambda_k\})) &= \sum_i N_i \log \, \Lambda(\{\lambda_k\}) - \sum_i \Lambda(\{\lambda_k\}) - \sum_i \log \, N_i! = \\ &= \sum_i N_i \log \, \Lambda(\{\lambda_k\}) - \sum_i \Lambda(\{\lambda_k\}) \end{aligned} \tag{3.12}$$

Here, we can omit the constant term $\sum_i \log \, N_i!$, since it is independent of the model parameters. Typically, the bins are contiguous, and we define the region of interest (ROI) to be the portion of the total data (the volume of phase space) we have selected. As a result this facilitates the introduction of unbinned Poisson likelihood, in which the bin widths are taken to be infinitesimal, such that only 0 or 1 counts can possibly be observed. This formulation sacrifices no information to binning but can become prohibitive for large data sets. Let P be the pixel set where $N_i = 1$, if we have a

small enough pixel Eq. 3.9 becomes $\Lambda_i(\{\lambda_k\}) = J(E_i, \hat{p}, \{\lambda_k\})\Delta t \Delta\hat{p}\Delta E$, so Eq. 3.12 yields

$$\begin{aligned}\log \mathscr{L}(\{\lambda_k\}) &= \sum_{i\in P} \log\, \Lambda(\{\lambda_k\}) - \sum_l \Lambda_{tot}(\{\lambda_k\}) = \\ &= \sum_{i\in P} \{\log\, J(E, \hat{p}, \{\lambda_k\}) + \log\, \Delta\hat{p} + \log\, \Delta E\} - \Lambda_{tot}(\{\lambda_k\}) = \\ &= \sum_{i\in P} \log\, J(E, \hat{p}, \{\lambda_k\}) + \Delta t^{N_{obs}} + \Delta\hat{p}^{N_{obs}} + \Delta E^{N_{obs}} - \Lambda_{tot}(\{\lambda_k\})\end{aligned} \tag{3.13}$$

Being the mid terms independent from the model they can be neglected for the likelihood maximization and Eq. 3.13 becomes

$$\log \mathscr{L}(\{\lambda_k\}) = \sum_{i\in P} \log\, J(E, \hat{p}, \{\lambda_k\}) - \Lambda_{tot}(\{\lambda_k\}) \tag{3.14}$$

The likelihood profile around the maximum provides an estimate of the statistical errors affecting the best-fit parameters. According to Cramer-Rao's disequation (Cramer, 1946; Rao, 1945) an upper limit to the covariance matrix terms is given by

$$\sigma^2_{ab} = \left\{ -\frac{\partial^2 \log \mathscr{L}}{\partial\lambda_a \partial\lambda_b}\bigg|_{\bar{\lambda}_k} \right\}^{-1} \tag{3.15}$$

Often one wants to quantify the level of agreement between the data and a hypothesis without explicit reference to alternative hypotheses. For example if we want to test two model: one without an additional source and the other with the additional source at a specified location. This can be done by using the likelihood ratio test (LRT), defining a test statistic TS, which is a function of the data whose value reflects in some way the level of agreement between the data and the hypothesis. Let us assume the hypothesis $\mathscr{H}$ of having a model $\mathscr{M}$ with $\{\lambda_k\}_{k=1,\cdots,m}$ free parameters, described by $\mathscr{L}$, and the hypothesis $\mathscr{H}_0$ of having a model $\mathscr{M}_0$ with $\{\lambda_k\}_{k=1,\cdots,h}$ free parameters, where $(h < m)$, described by $\mathscr{L}_0$. According to S. S. Wilks (1938 [58]) in the limit of a large number of counts the test statistic

$$TS = -2(\log \mathscr{L}_0 - \log \mathscr{L}) \tag{3.16}$$

is distributed asymptotically as a χ^2 with $(m-h)$ degrees of freedom. Staying in the context of testing two models without or with a new source, the number of additional parameters characterizing the χ^2 distribution are typically the ones of the new source. This means that TS is drawn from this distribution if no source is present, and an apparent source results from a fluctuation. Thus, a larger TS indicates that the null hypothesis is incorrect (i.e., a source really is present), which can be quantified. As a basic rule of thumb, the square root of the TS is approximately equal to the detection significance for a given source.

3.4.2 *Fermi Tools* Likelihood Analysis

We use a Python script for computing the Unbinned Likelihood analysis. We use as event data file fits `ft1.fits`, as spacecraft data file `ft2-30s.fits`[6], also referred to as the "pointing and livetime history" file, and the current background models `gll_iem_v06.fits` and `myEXT_iso_P8R2_SOURCE_V6_v06.txt` [7] We compute the following step:

[6] you can find both of them in my slac account:/afs/slac.stanford.edu/u/gl/denisec/script/fits/
[7] in /nfs/farm/g/glast/u/buson/diffuse/

Make Subselections from the Event Data

Since there is a computational overhead for each event associated with each diffuse component, it is useful to filter out any events that are not within the extraction region used for the analysis. To do this, we use `gtselect` tool[8]. We also selected the energy range and the maximum zenith angle value (90 degrees). The Earth's limb is a strong source of background gamma rays. We filter them out with a zenith-angle cut. The value of 90 degrees is the one recommended by the LAT instrument team for analysis above 100 MeV. We summarise the selected cut in Table 3.3. We use the selected time interval of the fits file in which we found the cluster position as Start Time(MET) and Stop Time(MET) parameter. For example, if we test a cluster position that we found in a 30 days analysis, then we use the same time range in the likelihood analysis.

Parameter	Value
Search Center	(RA, DEC)
Radius	10°
E_{min}	10 GeV
E_{max}	1 TeV
Event Class	SOURCE
Maximum Zenith Angle	90°

Table 3.3: Selection data for the Unbinned Likelihood Analysis.

After the data selection is made, we need to select the good time intervals in which the satellite was working in standard data taking mode and the data quality was good. A Good Time Interval (GTI) is a time range over which the data may be considered valid, and this extension is made part of the processed event file. Generally, it is desirable for the GTI to filter out events where the spacecraft is located physically in the South Atlantic Anomaly (SAA). The SAA is a region located over South America, above the South Atlantic Sea, and Africa where the LAT is exposed to a high flux of charged particles, due to the geomagnetic fields of the earth, and is not taking data. In orbit, the LAT crosses over the SAA 15% of the time.
The science tool `gtmktime`[9] is used to update the GTI extension and make cuts based on spacecraft parameters contained in the spacecraft (pointing and livetime history) file. It reads the spacecraft file and, based on the filter expression and specified cuts, creates a set of GTIs. These are then combined (logical `and`) with the existing GTIs in the Event data file, and all events outside this new set of GTIs are removed from the file. New GTIs are then written to the GTI extension of the new file. We made the current expression recommended by the LAT team `(DATA_QUAL>0)&&(LAT_CONFIG==1)`.

Make Counts Maps from the Event Files

Next, we create a counts map of the ROI, summed over photon energies, in order to identify candidate sources and to ensure that the field looks sensible as a simple sanity check. For creating the counts map, we will use the `gtbin`[10] tool with the

[8] `http://fermi.gsfc.nasa.gov/ssc/data/analysis/scitools/help/gtselect.txt`
[9] `http://fermi.gsfc.nasa.gov/ssc/data/analysis/scitools/help/gtmktime.txt`
[10] `http://fermi.gsfc.nasa.gov/ssc/data/analysis/scitools/help/gtbin.txt`

option CMAP.

Create a source model XML file

We create the source model XML (short for e**X**tensible **M**arkup **L**anguage) file, which contains the various sources and their model parameters to be fit.

Make an exposure map

Since we are interested in analysing the spectrum of a single source, we use the counts within a region around the source of interest. Nearby sources will contribute photons to this region, and we will probably want to model them. That is, to model a single source we may be forced to model a handful of sources. And therefore we may need to include counts from an even larger region.
However, the influence of sources fade with distance, thus, we should include sources from a large "Source Region" and counts from a smaller "Region of Interest" (the ROI). The positions and spectra of sources in the Source Region outside of the ROI must have been obtained previously, for example from a catalog; we include these sources for their contribution to the counts in the ROI.
The exposure calculation that the likelihood computation uses consists of an integral of the total response over the entire ROI:

$$\epsilon(E', \hat{p}') = \int_{ROI} dE d\hat{p} dt dR(E, \hat{p}|E', \hat{p}', t) \tag{3.17}$$

This exposure function can then be used to compute the expected numbers of events from a given source:

$$N_{pred} = \int dE' d\hat{p}' S_i(E', \hat{p}') \epsilon(E', \hat{p}') \tag{3.18}$$

where $S_i(E', \hat{p}')$ is the photon intensity from source i.
There are two tools needed for generating exposure maps.

- `gtltcube`[11], a tool is used to make a livetime cube, also known as an exposure cube, taking as arguments the FT1 and FT2 files, the desired bin size in degrees per pixel, and the cosine of inclination angle.
  In fact every time a gamma ray interacts in the LAT, causing a trigger, further data taking is disabled until data from the event are read out. The number of counts that a source should produce is therefore dependent on the amount of time that the source spent at a given inclination angle during an observation. This livetime quantity, the time that the LAT observed a given position on the sky at a given inclination angle, depends only on the history of the LAT's orientation during the observation and not on the source model. Thus the array of these livetimes at all points on the sky is called the "ivetime cube", a *cube* because it is a function of three variables, two related with the directions of the incoming photons and the inclination angle it hit the LAT.

- `gtexpmap`[12] creates an exposure map based on the event selection used by the input photon file and the livetime cube.

[11] `http://fermi.gsfc.nasa.gov/ssc/data/analysis/scitools/help/gtltcube.txt`
[12] `http://fermi.gsfc.nasa.gov/ssc/data/analysis/scitools/help/gtexpmap.txt`

Compute the diffuse responses

The diffuse source responses are computed by the `gtdiffrsp`[13] tool. The source model XML file must contain all of the diffuse sources to be fit. gtdiffrsp will add one column to the event data file for each diffuse source. The diffuse response depends on the instrument response function (IRF), which must be in agreement with the selection of events, i.e. the event class and event type we are using in our analysis.

Perform the Likelihood Fit

Using `gtlike`[14] tool we fit the data to the model, providing flux, uncertainties, spectral indices, and other information. There are five optimizers from which to choose: DRMNGB, DRMNFB, NEWMINUIT, MINUIT and LBFGS. We use the NEWMINUIT optimizer to find more accurate results, as used by the *Fermi* LAT team for most of the analyses.

Make the Residual Map

Before we compute a residual map, we need as well to follow the path of the binned likelihood analysis. Thus we perform the following steps:

- using `gtexpcube2` tool, we generate an exposure map, or a set of exposure maps for different energies, from a livetime cube written by `gtltcube`
- using `gtsrcmaps` tool, we create a model counts maps, binned in space and energy for each source of our xml model

After this steps we use the `gtmodel` tool, which creates a model map of a region based on the fit parameters, and we run again the `gtbin` tool with the CCUBE option using as a model the one created in the previous passage. Finally, we can compute the residual map by using the `farith`[15] to check if we can improve the model.

Make Test-Statistic Maps

Finally, using `gttsmap`[16], we calculate the TS map for the source localization and its detection. The resulting map can be used to localize sources within the analysis region. The TS maps are created by moving a putative point source through a grid of locations on the sky and maximizing the likelihood, actually minimising its minus logarithm, at each grid point, with the other, stronger, and presumably well-identified sources included in each fit. New, fainter sources are then identified as local maxima in the TS map.

The best cluster position

After the Unbinned Likelihood analysis is done, if we obtain for a cluster position which is not in correspondence with a known catalog source a TS greater than 25, we select this position as a trial for a new source, and we run the `gtfindsrc` tool[17] to determine the pointer source's optimized position.

[13] `http://fermi.gsfc.nasa.gov/ssc/data/analysis/scitools/help/gtdiffrsp.txt`
[14] `http://fermi.gsfc.nasa.gov/ssc/data/analysis/scitools/help/gtlike.txt`
[15] `http://fermi.gsfc.nasa.gov/ssc/data/analysis/scitools/help/farith.txt`
[16] `http://fermi.gsfc.nasa.gov/ssc/data/analysis/scitools/help/gttsmap.txt`
[17] `http://fermi.gsfc.nasa.gov/ssc/data/analysis/scitools/help/gtfindsrc.txt`

Chapter 4

Results

The clustering algorithm allows us to identify photons which are likely to be emitted by known sources, at least taking into account their direction and their uncertainties. In Section 4.1 we report the studies of time variability of some FSRQ sources, cataloged in TeVCat.
While in Section 4.2 we test our algorithm and check if it is able to point out specific flares already detected by the *Fermi* LAT Collaboration.
In Section 4.3, we show the results given by the Unbinned Likelihood analysis for a restrictive sample of clusters, looking at data set binned in cut on time intervals of 30 days and, in particular, we show that this method identified two new sources which are not present in any *Fermi* catalogs.
We point out that we do not analyse a cluster position within the clusters list obtained by the analysis of the data set containing all photons collected in 7 years, because of the difficulties explained in Section 3.2.2. In fact, we are still working at building a faster algorithm in order to choose proper clusters that could be likely associated with sources.

4.1 TeVCat Catalogue Sources

We studied few FSRQs (flat-spectrum radio quasars) of the TeVCat catalogue sources. This first step has a double aim. First of all we apply the same condition we used in order to build clusters, namely, if a photon has an angular distance from a source less than the sum of its CA95% value (the photon uncertainty in the direction) and the positional uncertainty of the source, then we associate this photon to the known source.In this way we could remove from the list the photons that most likely originated from known sources. The second aim is to observe the variability in time of known sources.
Figure 4.1 represents histograms of temporal variation of some FSRQs and it shows if a flare is detected by other Telescope during a multiwavelength observations. In particular, we reported if the flare is significantly detected for energies around few TeV by a Cherenkov Telescope such as MAGIC, HESS or VERITAS.
We study the temporal variability of the sources described in the paragraphs below.

4.1.1 4C +21.35

4C +21.35 (also known as PKS 1222+216, z = 0.432; Osterbrock & Pogge 1987 [49]) is a lobe dominated FSRQ at long radio wavelengths and a known γ-ray emitter (Tanaka et al. 2011 [53]; Ackermann et al. 2014 [9]).
Fermi LAT reported an increased γ-ray activity from the source during April 2009

(Longo et al. 2009[1]). Since December 2009 till mid 2010, it has been particularly active at γ-ray energies undergoing frequent and rapid flux variations (Ciprini 2009[2]). As you can see in Figure 4.1 during this period the source showed two prominent γ-ray flares ($> 10^{-5} ph\, cm^{-2} s^{-1}$): one in April 2010, 55313 in MJD (Donato 2010 ATel #2584) and another in June 2010, 55364 in MJD (Iafrate et al. 2010 [3]), the brightest so far in LAT band from this source (Kushwaha et al. 2014 [38]). A detailed investigation of LAT data during April flare confirmed VHE emission (129 GeV photon; Neronov et al. 2010[4]) leading to the inclusion of PKS 1222+216 in the LAT VHE catalog (Neronov et al. 2011 [48]).
During this high γ-ray activity period, the MAGIC observatory detected two VHE excesses, one immediately after the end of the April flare on MJD 55319.97 (Ackermann et al. 2014 [9]) and other one during the rising part of the June 2010 flare (Mose Mariotti 2010[5]; Aleksić et al 2011 [13]). Moreover also AGILE detected an increasing γ-ray flux above 100 MeV on May 2010[6].
After that intense and rapid flaring episodes in the γ-ray band, this source showed a persistent VHE emission detected with VERITAS on March 2014. It was detected at $\sim$6 standard deviations, and the flux level was preliminary estimated as 3% of the Crab Nebula above 100 GeV [7].

4.1.2 PKS 1441+25

PKS 1441+25 is another FSRQ, located at redshift $z = 0.939$ (Shaw et al. 2012, [52]). In Figure 4.1 we point out the double detection of this source by MAGIC (Mirzoyan R. 2015 ATel #7416) and VERITAS telescope (Mukherjee 2015 ATel #7433). MAGIC observed this source on 17/18 April 2015 and for $\sim$ 4 hours on 18/19 April 2015. The flux above 80 GeV is estimated to be about $8e^{-11} cm^{-2} s^{-1}$ (16% of Crab Nebula flux). After that also VERITAS detected VHE γ-ray emission during the night of April 21, 2015.

4.1.3 PKS 1510-089

The FSRQ PKS 1510-089 ($z = 0.360$) is known to be one of the most powerful astrophysical objects with a highly collimated relativistic jet and with a semi-angle aperture for the jet $\sim 0.2^\circ$ (Jorstad et al. 2005 [34]). Since the angle between the relativistic jet and the observer's line of sight $\sim 1.4^\circ$–3°, the jet almost coincides with the observer's line of sight (Homan et al. 2002 [33]).
From Figure 4.1 it follows that *Fermi* LAT detected several flares from the source, as on 12 January 2009 (MJD 54843) 4 January 2010 (MJD 55200), on 17 October 2011 (MJD 55851) (Hungwe et al., 2011, ATel #3694; Kataoka et al., 2008 [35]; Cabrera et al., 2013 [22]). Since the *Fermi* LAT detected a photon of $0.1\, TeV$ we highlight this interesting flare on 12 January 2009 (MJD 54843), which Cherenkov Telescope did not see.
The *Fermi* LAT collaboration detected also two flaring episodes centred on MJD 54917 and MJD 54962, in which the source underwent strong outbursts ($F > 5 \times 10^{-6} ph\, cm^{-2} s^{-1}$ above 100 MeV) for which the 1 day averaged flux above 100 MeV reached or even exceeded in few occasions $10^{-5} ph cm^{-2} s^{-1}$ (Tavecchio et al.,

[1] Longo, F., Giroletti, M., & Iafrate, G. 2009, ATel #2021
[2] Ciprini, S. 2009, ATel #2349
[3] ATel #2687
[4] Neronov, A., Semikoz, D., & Vovk, I. 2010, ATel #2617
[5] Mariotti, M. 2010, ATel #2684
[6] Bulgarelli et al., 2010, ATel #2641
[7] Holder J., 2014 ATel #5981

2010 [55]). This first one was detected by HESS on 26 March 2009 (MJD 54916) (Abramowski A. et al., 2013 [3]). MAGIC also detected this source twice. The first one on 19 February 2012 (MJD 55876), which followed the communication from the *Fermi* LAT that the source underwent spectral hardening in MeV-GeV range and ATel #3907 announcing enhanced γ-ray emission observed by AGILE on February 2nd (Cortina J., 2012, ATel #3965). The second one on 18 May 2015 (MJD 57160), reported an increase in the VHE ($> 100\,GeV$) γ-ray flux from this source and a preliminary analysis data taken from 2015/05/18 to 2015/05/19 shows a highly significant signal and a flux of $\sim 20\%$ from that of the Crab nebula above 100 GeV. In this period the source was also active in the high energy γ-ray band as seen by Fermi-LAT [8]. (Mirzoyan R., 2015, #7542)

4.1.4 S4 0954+65

The FSRQ S4 0954+65 is a γ-ray loud object at $z \sim 0.368$ (Landoni et al., 2015 [39]).
In Figure 4.1 the MAGIC telescopes detected very-high-energy (VHE; $E > 100\,GeV$) emission on 13/14 February 2015 (MJD 57067) reported by Mirzoyan on ATel #7080. This coincided with the detection of an unusually hard γ-ray ($E > 0.1\,GeV$) spectrum with a power-law photon index of (1.8 ± 0.1) by *Fermi* LAT (Tanaka et al., 2016 [54]) along with an elevated γ-ray flux (Ojha et al. 2015, ATel #7093).

4.1.5 3C 279

3C 279 is the first FSRQ detected in VHE γ-rays by the MAGIC telescope (MAGIC Collaboration et al. 2008 [12]). It is known to vary strongly over the entire electromagnetic spectrum (Paliya et al., 2015 [50])In Figure 4.1 we show that during December 2008 to April 2009 (the first green highlighted peak) the source entered a bright GeV γ-ray state, as observed by *Fermi* LAT (Ciprini et al. 2008 ATel #1864). MAGIC observations started on December 9, 2008 unfortunately 3C 279 could only be observed at zenith angles larger than 46° and for a short time (∼10 min) due to visibility constraints. These short runs were insufficient to detect the source. Follow-up observations were conducted at the end of December 2008 until April 2009 under more favorable zenith angles (smaller than 35°). However, no major increase in the optical or X-ray flux was seen simultaneously to the VHE γ-ray flare, because in January 2009 the source was observed by MAGIC during a low optical-X-ray state (Aleksić et al. 2011 [14]).
Also in the spring of 2011 when 3C 279 was showing increasing optical flux, as well as increased γ-ray flux as observed by *Fermi* LAT, the MAGIC observations did not yield in a detection. In fact the MAGIC observations missed the largest γ-ray peak but provided tighter upper limits at VHE with respect to previous MAGIC observations performed in 2009 (Aleksic et al. 2011B).
Then *Fermi* LAT detected the source in an extremely bright state in 2013 December (Buson 2013, ATel #5680) and in 2014 April. We denote the period from 2013 December 14 to 2014 January 3 (MJD 56640−56660) as high activity phase. In which it was observed not only an extremely bright γ-ray flare, but also it was detected an extremely hard γ-ray spectrum (Paliya et al., 2015 [50]).
After that on 16 June 2015 (57181 MJD), *Fermi* LAT observed a giant outburst from the flat spectrum radio quasar 3C 279 with a peak $> 100\,MeV$ flux of $\sim 3.6 \times 10^{-5}\,photons\,cm^{-2}s^{-1}$ averaged over orbital period intervals.

[8] `http://fermi.gsfc.nasa.gov/ssc/data/access/lat/msl_lc/source/1510-089`

4.1.6 3C 454.3

The FSRQ 3C 454.3 is a well known active galactic nucleus (AGN), but it is not a source detected yet by Cherenkov telescopes, this is why it is not listed in the TeVCat. It shows very bright flaring activities across the electromagnetic waveband (Britto et al., 2015, [19]), and since it was always detected during any AGILE pointing, made it earn the nickname of *Crazy Diamond*.
Despite its bright flaring activity it is not detected by a Cherenkov Telescope, due to its large redshift of $z = 0.859$ (Lynds, 1967 [41]). However, since the *Fermi* LAT Collaboration was able to pre-alert Cherenkov Telescopes that S3 0218+35 source (known also as B0218+357) was undergoing a flare. This source, with a redshift of $z = 0.944$ (Cohen et al., 2003 [24]), could be detected by Cherenkov Telescopes thanks to the gravitational lensing effect, which produced an *echo* delayed by 11 days. For this reason we are confident that also 3C 454.3, at a similar redshift but much more bright than S3 0218+35, will be soon listed in the TeVCat. Thus it is interesting to show its temporal behaviour, as you can see in Figure 4.1.

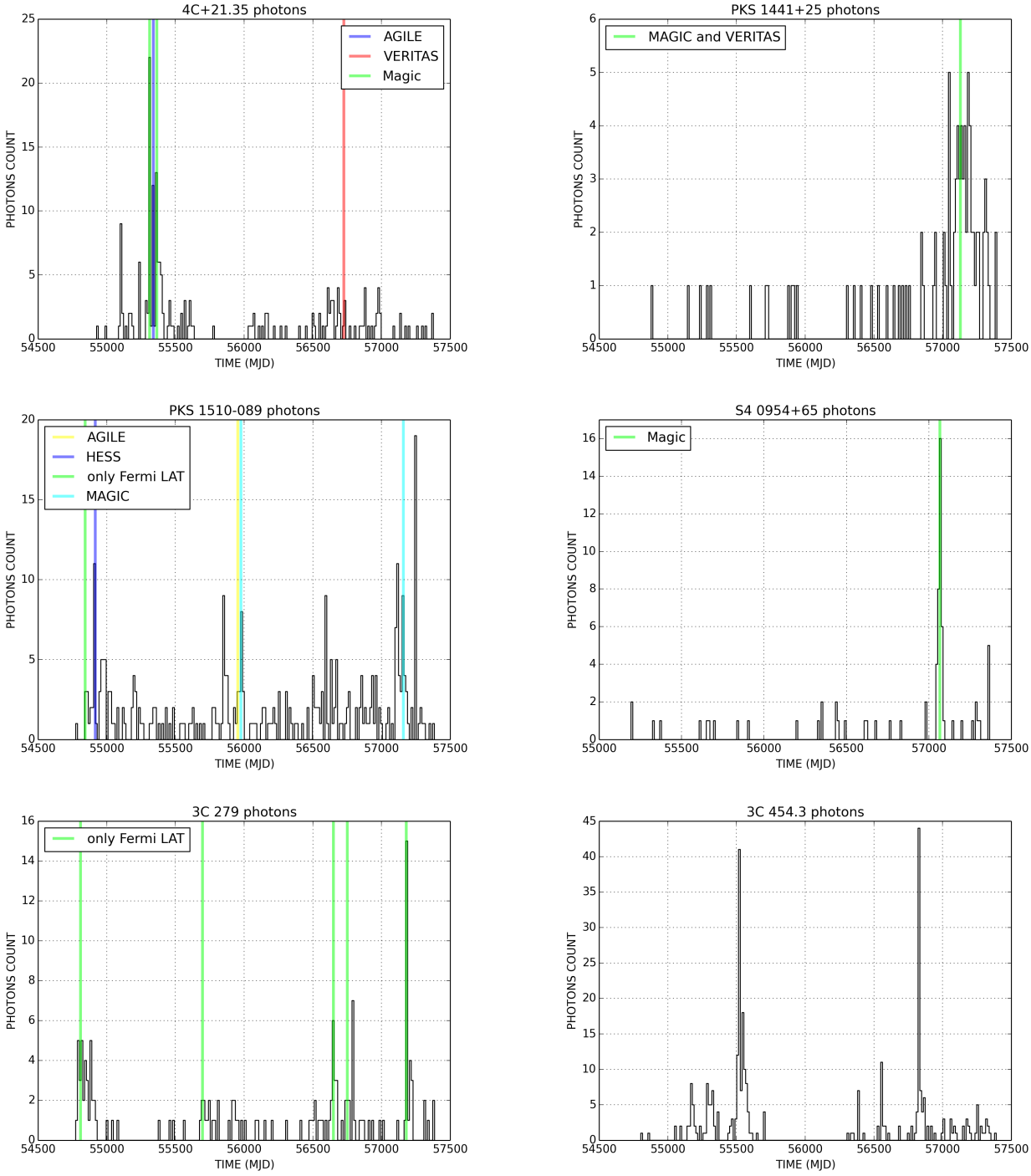

Figure 4.1: Temporal variability of 4C +21.35, PKS 1441+25, PKS 1510-089, S4 0954+65, 3C 279 FSRQ of TeVCat Catalogue, plus the analysis of 3C 454.3 source which is a FSRQ of 2FHL catalogue. We highlight flares detected by *Fermi* LAT and other Telescope during a Multiwavelength Observations. In particular we point out if a flare is significantly detected for energy around few TeV by a Cherenkov Telescope such as MAGIC, HESS or VERITAS.

4.2 Known identified Flares

Then we check if we are able to identify known flares, identified by the *Fermi* LAT collaboration.

4.2.1 B0218+357

We analyse a time range of less that 30 days, in such a way that we do not have the problem of duplicate clusters in different positions. We selected a time range of two days, with a MET ranging from 426954901 to 427127701. In this data range we detected the blazar B0218+357. It was detected for the first time in γ-rays by the *Fermi* LAT (Buson et al., 2015 [21]) and was the first ever gravitationally lensed blazar detected in the VHE (Mirzoyan, 2014 [44].
We listed all the clusters associated with this source in Table 4.1, just as we remarked in Paragraph 3.2.2, we find a number of identical clusters equal to the photons contained within the cluster. We note that the cluster's radius, or rather the dispersion at 66% from the mean cluster position, is included between $[0.05° - 0.11°]$, thus the region from which photons are emitted is really compact and we can safely assume that they are emitted from this source.
The final result given by an Unbinned Likelihood analysis of the cluster position (RA= 35.28°; DEC= 35.94°) are: $TS = 653.79$; $LogLike = -2656.85$; $Index = (-1.44 \pm 0.07)$. For this position we do not run `gtfindsrc` tool because it is already a catalogued source.

Photon Index	PSF_T	RA (deg)	DEC (deg)	NUM_PHS	RADIUS (deg)
74	psf2	35.21	35.93	12	0.07
491	psf3	35.21	35.93	12	0.07
19	psf3	35.21	35.93	12	0.09
222	psf2	35.21	35.93	12	0.09
78	psf3	35.21	35.93	12	0.05
186	psf1	35.21	35.93	12	0.11
79	psf3	35.21	35.93	12	0.07
185	psf0	35.21	35.93	12	0.11
138	psf2	35.21	35.93	12	0.06
14	psf2	35.21	35.93	12	0.11
390	psf1	35.21	35.93	12	0.09
252	psf3	35.21	35.93	12	0.11

Table 4.1: Clusters associate with B0218+357 source, looking at a time range of 2 days, between (426954901 - 427127701) in MET.

4.2.2 GRB 130427A

We subdivide the original data sample of about 7 year of collected data into smaller intervals of 30 days each. Then, we select the clusters that have smaller radii and a higher number of contained photons. With the first condition, we select clusters that have a small dispersion, thus the contained photons are more concentrate in a certain position, and with the second condition we choose clusters that are statistically more significant.
Figure 1.1 shows all clusters selected with this recipe, in particular we circle the cluster position that we studied. An example of the cluster parameters that we associate to this source are: (Photon Index=5288; PSF_T=psf3; RA= 173.15°; DEC= 27.71°; NUM_PHS=18; RADIUS= 0.13°).
We run an Unbinned Likelihood analysis for (RA= 173.18°; DEC= 27.79°) position, obtained after running `gtfindsrc` tool. We get: $TS = 197.87$; $LogLike =$

-705.687; $Index = (-1.65 \pm 0.05)$.

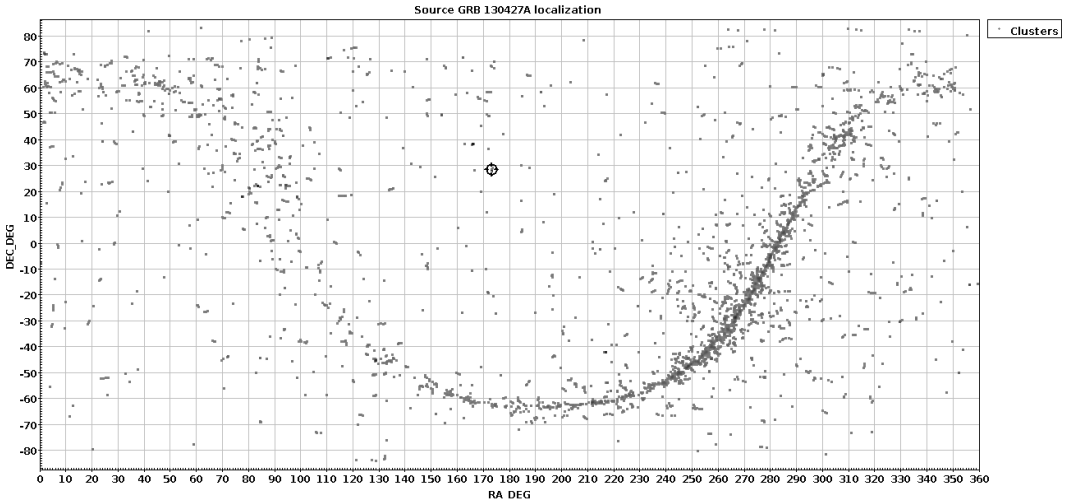

Figure 4.2: Clusters obtained by a data set with a range in time between [386968129 – 389560129] in MET. We highlight with a circle the GRB 130427A cluster localization (RA= 173.15°; DEC= 27.71°) with 18 photons within the cluster and a small radius 0.13°, thus a small dispersion.

4.3 New Sources

We point out possible clusters candidate that will be new, non catalogued, sources. As we do in Paragraph 4.2.2, we choose as a good *seed* for a candidate source the centres of the clusters that have smaller radii and a great number of photons. We then check the likelihood that these *seeds* are gamma-ray sources by computing the TS of the Unibinned Likelihood Approach used in *Fermi* LAT. From this list we detected two new candidate sources:

- **Clust1** is detected in the 30 days sample within [272920129-275512129] in MET. Its parameters are (PSF_T=psf1; RA= 265.03°; DEC= 27.40°; NUM_PHS=7; RADIUS= 0.14°).
  We run an Unbinned Likelihood analysis for (RA= 264.93°; DEC= 27.34°) position, obtained after running `gtfindsrc` tool. We get: $TS = 61.66$; $LogLike = -944.746$; $Index = (-1.90 \pm 0.09)$.
  The known gamma-ray source closer to this position is 3FGLJ1748.0+2701 (RA= 267.02°;DEC= 27.02°) (listed also in the new 3FHL which will be soon released), it is located at an angular distance of 1.88°.
  Figure 4.3 shows all clusters selected with this recipe, in particular we circle the cluster position that we studied.

- **Clust2** is detected in the 30 days sample within [441400129-443992129] in MET. Its parameters are (PSF_T=psf1; RA= 159.50°; DEC= 45.09°; NUM_PHS=4; RADIUS= 0.14°).
  We run an Unbinned Likelihood analysis for (RA= 159.58°; DEC= 45.16°) position, obtained after running `gtfindsrc` tool. We get: $TS = 30.22$; $LogLike = -847.70$; $Index = (-2.02 \pm 0.12)$. The closer gamma-ray source is B3 1009+427 (RA= 153.18°; DEC= 42.49°) (listed also in the new 3FHL), at an angular distance of 5.33°.

Figure 4.4 shows all clusters selected with this recipe, in particular we circle the cluster position that we studied.

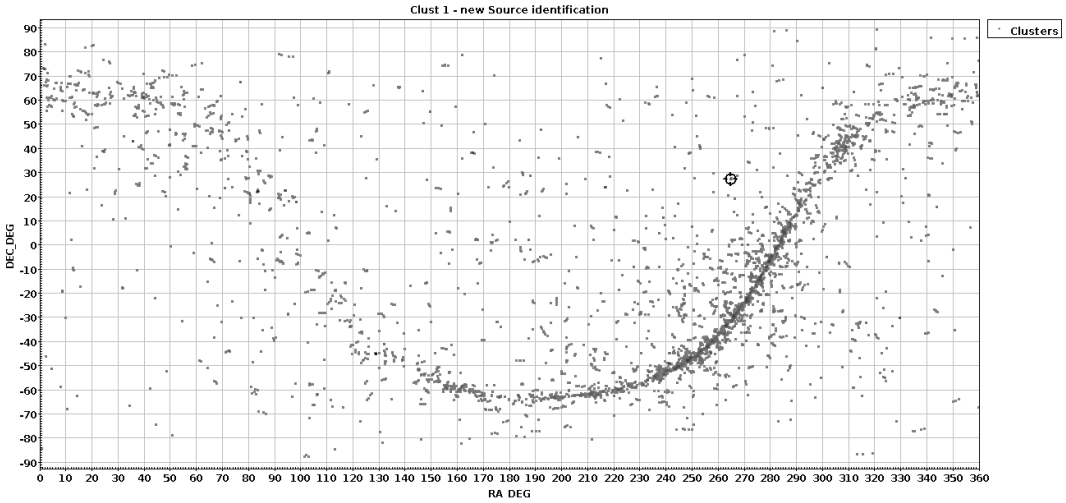

Figure 4.3: Clusters obtained by a data set with a range in time between [272920129-275512129] in MET. We highlight with a circle the cluster localization (RA= 264.93°; DEC= 27.34°) with 7 photons within the cluster and a small radius 0.14°, thus a small dispersion.

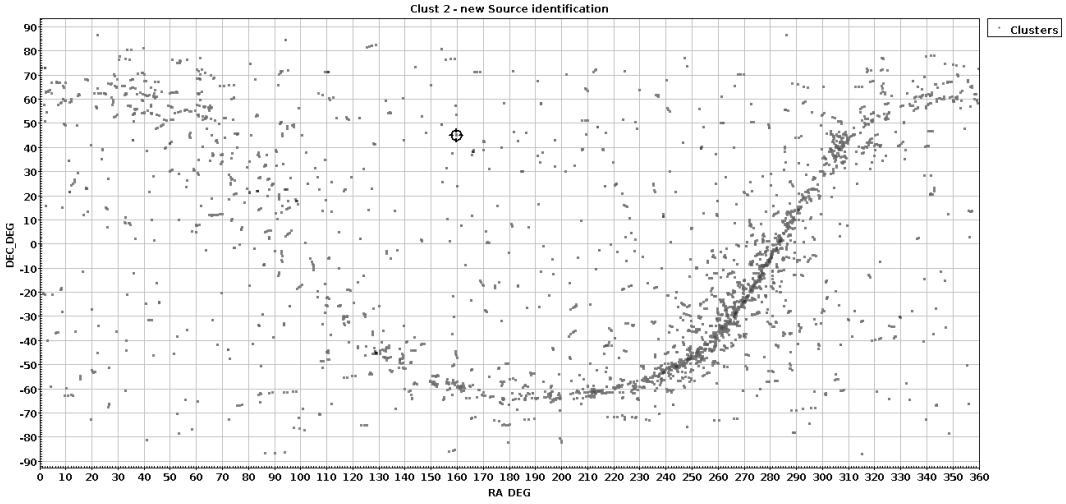

Figure 4.4: Clusters obtained by a data set with a range in time between [441400129-443992129] in MET. We highlight with a circle the cluster localization (RA= 159.50°; DEC= 45.09°) with 4 photons within the cluster and a small radius 0.14°, thus a small dispersion.

Chapter 5

Conclusion

The past decade has seen a dramatic improvement in the quality of data available at both high (HE, $> 10\,GeV$) and very high (VHE, $> 100\,GeV$) γ-ray energies. Thanks to the latest Pass8 data release by *Fermi* LAT which increases the overlap in energy coverage with Cherenkov Telescopes, we can extend the observation in γ rays until few TeV.
There are two main aims of this work: to identify new potential γ-ray sources: by focusing on the HE emission, we estimate which are the best candidates to be VHE emitters. The second aim is to study the temporal variations of the luminous flux of known HE sources.
During the thesis we developed, applied and tested a new time and spatial clustering algorithm, which is able to analyse the whole *Fermi* LAT data set (about 7 years) as well as study shorter-time interval datasets.
The method characterises the temporal variations of known VHE sources listed in TeVCat, albeit we restricted our study only to FSRQ sources, with the new approach described in Section 4.1: considering the uncertainty of the photon direction reconstructed by the *Fermi* LAT, the containment angle at 95%, and the uncertainty on the direction of the source under study as reported in the *Fermi* LAT catalogues.
To test our algorithm, we check if flares, already identified by the *Fermi* LAT Collaboration, are detected by our algorithm and, to assess the discovery potential of the method itself, we check whether flaring activities in HE is seen also at VHE during multiwavelength observations.
By dividing data into smaller data sets (typically 30 daya), it is able to identify additional flaring activities detected by the *Fermi* LAT Collaboration (Section 4.2) and, above all, new candiate sources (Section 4.3) which can not be detected by analysing the whole *Fermi* LAT data set (about 7 years), since their signal will be washed out in the long interval of time by decreasing signal-to-noise ratio.
The next improvements of our clustering algorithm will follow two parallel paths: look for a suitable method to merge clusters and to delete identical clusters, and to provide a better estimator of the cluster's dispersion, the radius, that, in this work, we identified empirically with the second tercile.
The first issue, as explained in Section 3.2.2, is a typical problem of partitional clustering algorithms, the class of algorithm to which our analysis belongs. In addition, our approach is complicated by the fact that the sample is moderately numerous, 704902 photons collected in about 7 years by *Fermi* LAT, and the resources in memory requested by the algorithm scale as N^2. Computations then are not easy in themselves, as the distance is a function that has to be evaluated in SO(3).
Regarding the second issue, we believe that we could better estimate the radius,

the *width* of our cluster, by exploiting the Rayleigh statistics (Fisher 1953 [27]; Briggs 1993[18]), and the more convenient form for large sample ($N \geq 50$), known as Rayleigh-Watson statistics W (Watson 1956, 1983 [57]). Let us look at the value $R = |\sum_i r_i|$ with $i = 1, \cdots, N$, the module of the vectorial sum of the N directions of the photons within a single cluster (represented in rectangular coordinate by (x_i, y_i, z_i), with $x_i^2 + y_i^2 + z_i^2 = 1$). If the directions are isotropically distributed, versors, on average, tend to cancel each other and the resulting R will be close to zero, while if there is an actual asymmetry R will tend to be larger than expected for the isotropic distribution.
In a sense, R is lower the more our data are *contaminated* by the isotropic component. In more detail, we see that in a cluster of N photons isotropically distributed, computing R is actually performing a random-walk process of N unit steps and R is the final distance from the origin. A well-known result from the random-walk theory then states that $< R^2 >= N$, where

$$\rho = R^2 = (\sum_i x_i^2) + (\sum_i y_i)^2 + (\sum_i z_i)^2 \tag{5.1}$$

from which it follows the Rayleigh-Watson statistics, defined as $W = R^2(3/N)$, where $< W >= 3$ is asymptotically distributed as χ^2 distribution with three degrees of freedom (Agati et al., 2015 [10]).
Thus, we are confident that ρ in Equation 5.1, or better its value normalized with a function of N, could be a good *estimator* of both the width of the cluster used in the merging process and of the contamination of the isotropic component.
Detailed Monte Carlo simulations will ensue in order to characterise the bahaviour and the potentiality of ρ.

Bibliography

[1] Abdo, A.A. et al. *The on-orbit calibration of the Fermi Large Area Telescope*, 2010, Astroparticle Physics, 32, 193. 0904.2226

[2] Abdo A.A., Ackermann M., Agudo I.,Ajello M., et al. *The Spectral Energy Distribution of Fermi Bright Blazars*, 2010, ApJ, `http://arxiv.org/abs/0912.2040`

[3] Abramowski A. et al. (HESS Collaboration) *H.E.S.S. discovery of VHE γ-rays from the quasar PKS 1510-089*, 2013, A&A, 554 `arXiv:1304.8071`

[4] Acero F. et al. *Fermi Large Area Telescope Third Source Catalog*, 2015, ApJS, `http://arxiv.org/abs/1501.02003v3`

[5] Ackermann, M. et al. *The Fermi Large Area Telescope On Orbit: Event Classification, Instrument Response Functions, and Calibration*, 2012, Astroparticle Physics, 203 `doi:10.1088/0067-0049/203/1/4`

[6] Ackermann, M. et al.*Determination of the Point-Spread Function for the Fermi Large Area Telescope from On-orbit Data and Limits on Pair Halos of Active Galactic Nuclei*, 2013, The Astrophysical Journal, `arXiv:1309.5416`

[7] Ackermann M. et al. *2FHL: The Second Catalog of Hard Fermi-LAT Sources*, 2015, ApJ, `10.3847/0067-0049/222/1/5`

[8] Ackermann M. et al. *3FHL: The Third Catalog of Hard Fermi-LAT Sources*, in preparation

[9] Ackermann, M., Ajello, M., Allafort, A., et al. *Multifrequency Studies of the Peculiar Quasar 4C +21.35 during the 2010 Flaring Activity*, 2014, ApJ, 786, 157

[10] Agati J. L. et al. *Are the orbital poles of binary stars in the solar neighbourhood anisotropically distributed?*, 2015, A&A 574, A6 `10.1051/0004-6361/201323056`

[11] Ajello et al. *The spectrum of isotropic diffuse gamma-ray emission between 100 MeV and 820 GeV*, 2014, `http://arxiv.org/abs/1410.3696`

[12] Albert, J., Aliu, E., et al. (MAGIC Collaboration) 2008, Science, 320, 1752

[13] Aleksić, J., Antonelli, L. A., Antoranz, P., et al. 2011, ApJ, 730, L8

[14] Aleksić et al. (MAGIC collaboration) *MAGIC observations and multiwavelength properties of the quasar 3C279 in 2007 and 2009* 2011 A&A 530, `arXiv:1101.2522`

[15] Atwood W.B., et al. *Design and initial tests of the Tracker converter of the Gamma-ray Large Area Space Telescope*, 2007, Astroparticle Physics, 28, 422.

[16] Atwood W.B., Abdo, Ackermann, et al. *The Large Area Telescope on the Fermi Gamma-Ray Space Telescope Mission*, 2009, ApJ, `http://arxiv.org/abs/0902.1089`

[17] Atwood, et al., *Pass 8: Toward the Full Realization of the Fermi-LAT Scientific Potential*, 2013, `arXiv:1303.3514`

[18] Briggs, M. S. 1993, ApJ, 407, 126

[19] Britto R. J. G, Buson S., Lott B., Razzaque S., Bottacini E. *Fermi-LAT Observations of 2014 May-July outburst from 3C 454.3*, 2015, The Astrophysical Journal `arXiv:1511.02280`

[20] Buson Sara, *The TeV AGN Portfolio: extending Fermi-LAT analysis into the CTA realm*, 2013, `paduaresearch.cab.unipd.it/5909/`

[21] Buson, S., Cheung, C. C., Larsson, S., & Scargle, J. D. *Fermi-LAT Detection of a Hard Spectrum Flare from the Gravitationally Lensed Blazar B0218+357* 2015, Proc. of 2014 Fermi Symposium, `arXiv:1502.03134`

[22] Cabrera J.I, Coronado Y., Benitez E., Mendoza S., Hiriart D., Sorcia M. *A hydrodynamical model for the FERMI-LAT γ-ray light curve of Blazar PKS 1510-089*, 2013, MNRA Letters, 434, `arXiv:1212.0057`

[23] Casandjian J.M and Grenier I.A., *A revised catalogue of EGRET γ-ray sources*, 2013, Astronomy & Astrophysics

[24] Cohen J.G., Lawrence C.R., Blandford R.D. *The Redshift of the Lensed Object in the Einstein Ring B0218+357*, 2003, ApJ, 583, `arXiv:astro-ph/0209457`

[25] Davis, J.E. *The Formal Underpinnings of the Response Functions Used in X-Ray Spectral Analysis*, 2001, Astrophys. J., 548, 1010. `arXiv:astro-ph/0011068`

[26] Fossati G., Maraschi L., Celotti A., Comastri A. and Ghisellini G. (1998). "A unifying view of the spectral energy distributions of blazars". MNRAS, 299:433–448. `http://adsabs.harvard.edu/abs/1998MNRAS.299..433F.37`

[27] Fisher R. *Dispersion on a Sphere*, 1953, Proc. Roy. Soc. A, 217, 295

[28] Funk S., Hinton J.A. *Comparison of Fermi-LAT and CTA in the region between 10–100 GeV*, 2013, Astroparticle Physics 43 348–355

[29] Giommi, Padovani et al., *A simplified view of blazars: clearing the fog around long-standing selection effects*, 2011

[30] Grove, J. E., & Johnson, *The calorimeter of the Fermi Large Area Telescope*, 2010, Proc. SPIE, 7732

[31] Harel D. and Koren Y. *Clustering Spatial Data Using Random Walks*, 2001, KDD, pp.281-286.

[32] Hartman R. C. et al. *The Third EGRET Catalog of High-Energy Gamma-Ray Sources*, 1999, ApJS, `123:79\OT1\textendash202`

[33] Homan D. C., Wardle J. F. C., Cheung C. C., Roberts D. H., Attridge J. M., *PKS 1510–089: A Head-on View of a Relativistic Jet*, 2002, ApJ, 580, 742

[34] Jorstad S. G., et al., *Polarimetric Observations of 15 Active Galactic Nuclei at High Frequencies: Jet Kinematics from Bimonthly Monitoring with the Very Long Baseline Array*, 2005, Astronomical Journal, 130, 1418

[35] Kataoka J., Madejski G., et al. *Multiwavelength Observations of the Powerful Gamma-Ray Quasar PKS 1510–089: Clues on the Jet Composition*, 2008, ApJ, 672, 787

[36] Kerr M., *Likelihood Methods for the Detection and Characterization of Gamma-ray Pulsars with the Fermi Large Area Telescope*, 2010, `http://arxiv.org/abs/1101.6072`

[37] King, I. 1962, AJ, 67, 471

[38] Kushwaha P., Singh K. P., Sahayanathan S. *Brightest Fermi-LAT Flares of PKS 1222+216: Implications on Emission and Acceleration Processes*, 2014, ApJ, 796, 61, `arXiv:1409.8201`

[39] Landoni M., Falomo R., Treves A., Scarpa R., Reverte Paya D. *What is the redshift of the gamma-ray BL Lac source S4 0954+65?*, 2015, The Astronomical Journal, 150, 6, `arXiv:1510.02087`

[40] Lynden Bell *Galactic Nuclei as collapsed old quasars*, 1969.

[41] Lynds C. R., 1967, ApJ, 147, 837

[42] Manfreda A. *Pass 8: development and science prospects for the new Fermi LAT event-level analysis*, 2014, `https://etd.adm.unipi.it/t/etd-06232014-150706/`

[43] Mattox et al., *The Likelihood Analysis of EGRET data*, 1996, `http://adsabs.harvard.edu/abs/1996ApJ...461..396M`

[44] Mirzoyan R., 2014 The Astronomer's Telegram #6349, `http://www.astronomerstelegram.org/?read=6349`

[45] Moiseev, A. A., Hartman, R. C., Ormes, J. F., Thompson, D. J., Amato, M. J., Johnson, T. E., Segal, K. N., & Sheppard, D. A. 2007, Astroparticle Physics, 27, 339

[46] Milotti V., *Space and Time Clustering of High-Energy Photons detected by the Fermi LAT*, 2014, `http://tesi.cab.unipd.it/47251/`

[47] Neyman, J., & Pearson, E.S., *On the Use and Interpretation of Certain Test Criteria for Purposes of Statistical Inference*, 1928, Biometrica, 20A, 175

[48] Neronov, A., Semikoz, D., & Vovk, I. 2011, A&A, 529, A59

[49] Osterbrock D. E., & Pogge R. W. *Optical spectra of narrow emission line Palomar-Green galaxies* 1987, ApJ, 323, 108, `10.1086/165810`

[50] Paliya V.S., Diltz C., Bottcher M., Stalin C.S., Buckley D. *A hard gamma-ray flare from 3C 279 in 2013 December*, 2015 ApJ `arXiv:1512.00203`

[51] Pollock, A.M.T., et al., 1981, A&A, 94, 116

[52] Shaw et al. *Spectroscopy of Broad-line Blazars from 1LAC* 2012, ApJ, 748, 49, `arXiv:1201.0999`

[53] Tanaka, Y. T., Stawarz, Ł., Thompson, D. J., et al. Fermi *Large Area Telescope Detection of bright γ-ray outburst from the peculiar quasar 4C +21.35* 2011, ApJ, 733, 19

[54] Tanaka et al. *A significant hardening and rising shape detected in the MeV/GeV nuFnu spectrum from the recently-discovered very-high-energy blazar S4 0954+65 during the bright optical flare in 2015 February*, 2015, Astronomical Society of Japan, `arXiv:1604.05427`

[55] Tavecchio F., Ghisellini G., Bonnoli G., Ghirlanda G. *Constraining the location of the emitting region in Fermi blazars through rapid gamma-ray variability*, 2010 MNRAS Letters `arXiv:1003.3475`

[56] Urry C.M. & Padovani P. *Unified Schemes for Radio-Loud Active Galactic Nuclei*, 1995, Phy. Rev. Lett. (Vol. 107), Publications of the Astronomical Society of the Pacific.

[57] Watson, G. 1956, Geophys. J. Int., 7, 160

[58] Wilk S. S. *The large-sample distribution of the likelihood ratio for testing composite hypotheses*, 1938, Ann. Math. Stat., 9, 60.

[59] Wilms J. et al. *XMM-EPIC observation of MCG-6-30-15: direct evidence for the extraction of energy from a spinning black hole?*, 2001, MNRAS, 328, L27.